Earthquake Engineering & Structural Dynamics

WILEY

RESEARCH ARTICLE OPEN ACCESS

Combined Vertical and Horizontal Components of Near-Source Earthquakes and Impact on Base-Isolated Structures

Giulia Giuliani[1] | Sara Sgobba[2] | Fabio Micozzi[1] | Fadel Ramadan[2] | Laura Ragni[3] | Giovanni Lanzano[2] | Lucia Luzi[2] | Andrea Dall'Asta[4]

[1]SAAD, University of Camerino, Ascoli Piceno, Italy | [2]Istituto Nazionale di Geofisica e Vulcanologia, Milano, Italy | [3]Department of Civil and Building Engineering and Architecture, Università Politecnica delle Marche, Ancona, Italy | [4]School of Science and Technology, University of Camerino, Camerino, Italy

Correspondence: Giulia Giuliani (giulia.giuliani@unicam.it)

Received: 20 August 2025 | **Revised:** 28 November 2025 | **Accepted:** 30 November 2025

Keywords: base-isolated structures | ground motion models | near-fault effects | near-source sites | vertical ground motion

ABSTRACT

Over recent decades, the collection of seismic data has improved the understanding of near-fault ground motion effects, which involve both horizontal and vertical components. Among the most significant effects are fault-normal directivity, which concentrates seismic energy into an intense, long-period pulse, and fault-parallel fling step, which causes permanent ground displacement. In dip-slip faulting scenarios (such as reverse and normal faults), significant vertical acceleration also occurs, as highlighted by recent studies, which have shown that vertical acceleration can exceed the horizontal component at short spectral periods. This research proposes a systematic approach to evaluate the combined effects of the vertical and horizontal components of near-fault ground motion – including pulse-like effects – for different near-source scenarios. The approach is applied to base-isolated structures equipped with high-damping rubber bearings (HDRBs), either alone or in combination with flat slider bearings (FSBs). The results, consistent with previous experimental and numerical studies on similar isolation systems, indicate that the vertical component does not influence the horizontal response of the hybrid isolation system or the superstructure, but it can cause uplift of FSBs, cavitation of HDRBs, and very large vertical accelerations in the superstructure. Furthermore, for scenarios similar to the one considered, they provide insight into the fault distances at which these phenomena may pose significant challenges for base-isolated buildings.

1 | Introduction

Characterising the seismic input for near-fault (NF) sites, located within approximately 15 km of the fault, requires particular considerations, as well as the evaluation of the structural response to that input. Over the past few decades, the extensive collection of seismic data has enhanced the understanding of near-fault ground motion effects, which encompass both horizontal and vertical components. One of the most significant near-fault effects is the fault-normal forward directivity, which occurs when the fault rupture propagates at a velocity comparable to the shear wave velocity [1]. This phenomenon concentrates seismic energy into a single, intense, and long-period pulse (bilateral velocity pulse). A second effect, the fault-parallel fling step, manifests as a unilateral velocity pulse, resulting in a permanent ground displacement. In dip-slip faulting scenarios (reverse and oblique faults), significant vertical acceleration also occurs due to the slip component along the vertical axis. All these effects are widely recognised in the literature [2–5]. Recently, particular attention has been given to the vertical component of earthquakes in

near-fault sites with dip-slip faults [6, 7], where the vertical peak earthquake component may also exceed the horizontal component. This phenomenon is particularly evident in the range of short spectral periods, around 0.05–0.1 s, where the spectral ratio (V/H) between vertical and horizontal pseudo-accelerations can exceed unity. This V/H ratio may be further amplified by sites with soft soil conditions [8]. Based on these studies, near-source ground motion models (GMMs) have been recently developed for defining both vertical and horizontal response spectra accounting for NF effects based on the NGA-W2 Database (for Western North America), as well as worldwide databases [9–12]. Recent seismic events, such as the 2016 Central Italy earthquake, highlighted the importance of the vertical component of NF records, even in the case of moderate-magnitude dip-slip faults (Mw = 6.5), and demonstrated the high vulnerability of structures, particularly masonry buildings, to the combined vertical and horizontal accelerations. Vertical accelerations recorded were, in fact, able to significantly reduce frictional resistance for a very short time, increasing the likelihood of sliding between bricks or stones due to the simultaneous impulsive horizontal acceleration [13].

The effects of NF earthquakes have also been extensively studied for base-isolated structures, since the use of this structural system (which can withstand strong earthquakes without loss of functionality) is increasingly common in high-seismicity areas, including regions near potential seismic faults. Additionally, advancements in isolation bearing technology have led to increased isolation periods, which consequently may coincide with long pulse periods of fault-normal ground motions, leading to a very high horizontal displacement demand. This effect has been widely investigated by several authors, as summarised in Erdik et al. [14]. More in detail, numerous studies have analysed the influence of pulse periods of the horizontal seismic component on structural response [15, 16], as well as the efficiency of added damping in controlling and mitigating the response [17, 18] or the effectiveness of increased isolator displacement capacity and superstructure strength in achieving an acceptable collapse risk [19, 20]. The effects of the vertical seismic component on the performance of base-isolated structures have also been investigated in the past, both regarding the vertical response (potential amplification of vertical axial forces and vertical accelerations) and its influence on the horizontal response of the isolation system (base shear) and superstructure (drifts and horizontal floor accelerations). It was found that the vertical seismic component can be adverse for all the most common kinds of isolation bearings, since they are all characterised by a high vertical stiffness in compression, thus the resulting vertical periods of base-isolated buildings fall within the critical range of vertical seismic spectra. Moreover, all of them commonly offer limited or no resistance to axial tensile force. Currently, friction pendulum systems (FPSs) and lead rubber bearings (LRBs) are the predominant isolation systems employed in regions with high seismicity, such as North America [21] and Turkey [22]. The popularity stems from their ability to provide a long isolation period and high energy dissipation, effectively reducing the displacement demands on the isolation system and the horizontal seismic action on the superstructure. In comparison, high-damping rubber bearings (HDRBs) offer lower energy dissipation and are typically employed alone in areas with moderate seismic risk, such as Italy [23, 24], or in conjunction with supplemental damping devices in high-seismic zones, such as Japan [23, 24]. Elastomeric bearings, including LRBs, HDRBs, and natural rubber bearings (NRBs), can withstand only modest tensile loads, while FPSs offer no resistance to axial tension. Consequently, as investigated in several past studies, FPSs may experience bearing decompression leading to temporary uplift [25], while elastomeric bearings may undergo rubber cavitation when the tensile stress exceeds the cavitation threshold [26]. Moreover, for FPSs, variations in axial load can significantly influence the horizontal response of all types of isolation bearings, affecting the force transmission to the superstructure. In this regard, an important experimental campaign has been conducted involving shaking table tests on a building structure equipped with triple friction pendulum (TFP) isolators with varying characteristics [27]. This study concludes that while the vertical input does not affect the horizontal displacement of the isolators, it has a significant impact on the base shear force, which must not be neglected in design considerations [28]. Another major test involving a full-scale building was carried out in both base-isolated and fixed-base configurations [29]. Both FPS and LRB systems have been used, and particular attention has been given to non-structural components. All these studies highlight the importance of the vertical component in the seismic response of the tested structural systems.

To date, there is no comparable experimental evidence for HDRBs, which are the subject of this paper. However, their vertical behaviour is similar to LRBs. Moreover, in recent years, some numerical investigations [30, 31] have been conducted in countries where they are used, driven by the growing awareness of the significance of the vertical component, especially in near-fault (NF) earthquake records. These studies show that the vertical component has little effect on the horizontal behaviour of the isolation system (base displacement and base shear). In contrast, axial forces in the bearings and vertical floor accelerations are significantly influenced. Nevertheless, these findings are based on highly simplified models of HDRBs, both in the horizontal and vertical directions. Currently, very advanced models are available for this type of isolator. In particular, models capable of reproducing both the complex load-history-dependent horizontal behaviour [32–34] and the tensile behaviour subject to cavitation [35] have been developed and implemented in advanced computational software such as OpenSees [35, 36], also very recently [37]. The load-history dependence, which leads to the so-called scragging or Mullins effect, plays an important role in assessing the seismic response of HDRBs and has even limited their application in certain cases [38]. However, this aspect has been disregarded in the present study, as the focus is on evaluating the effect of vertical ground motion. To this purpose, the model used in this work [39, 40] does not incorporate full load-history dependence and adopts a simplified post-cavitation behaviour. Nevertheless, it is capable of accurately simulating the coupled horizontal–vertical response under large horizontal displacements and high vertical compression loads. Moreover, the model, originally developed for Japanese bearings, has been slightly modified by the authors [41, 42] to better reproduce the experimental behaviour of HDRBs used in Europe under large deformations and axial loads. Additionally, following current European practice, in this study, HDRBs have been used in combination with low-damping flat sliding bearings (FSBs) to create a hybrid isolation system, which is an effective solution, as verified also by recent experimental investigations [43].

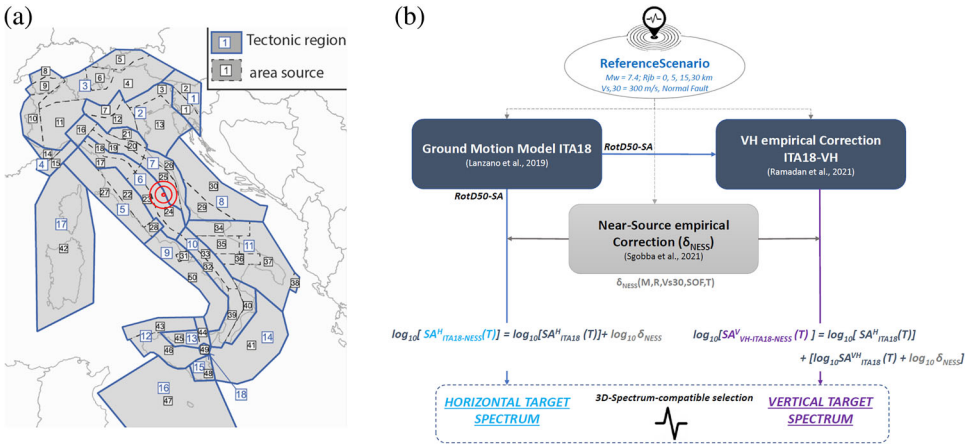

FIGURE 1 | The Italian zonation proposed by Visini et al. [52] and the selected site (concentric circles representing the considered fault distances) (a), and a flow chart depicting the spectra generation procedure (b).

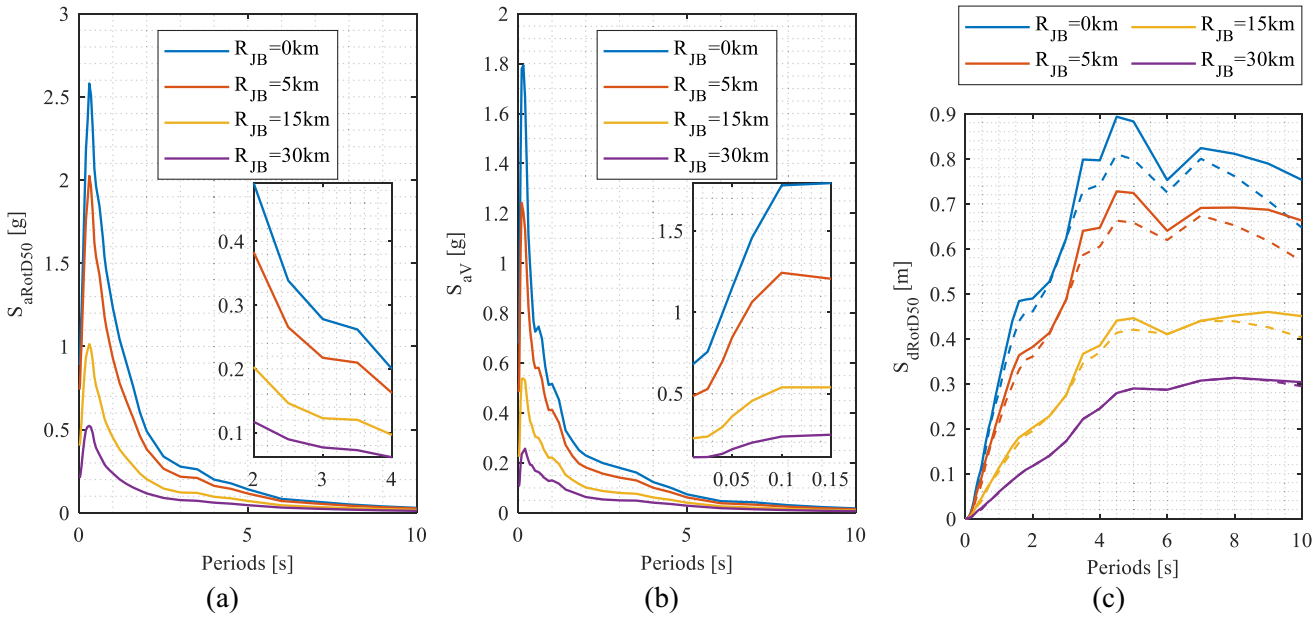

FIGURE 2 | Horizontal (a) and vertical (b) response spectra in terms of pseudo-acceleration and (c) horizontal response spectra in terms of displacement.

In particular, this paper presents a systematic analysis based on a probabilistic framework incorporating an appropriate selection of three-dimensional ground motions and delivering a quantitative assessment of the impact of near-fault (NF) ground motions. The methodology involves defining appropriate scenarios, deriving target spectra from the selected GMMs, and implementing a rational and rigorous ground motion selection process. This study defines spectra relevant to specific near-source conditions based on a recently proposed GMM [10], which leverages a comprehensive ground motion database that adequately covers the range of near-fault signals. The GMM accounts also for near-fault effects [11] and the V/H ratio [12]. Four seismic scenarios are analysed in this paper, assuming Joyner–Boore distances of 0, 5, 15, and 30 km, and an earthquake magnitude of Mw = 7.4 (typical of high-seismicity areas in Italy), to compare the different responses. A selection procedure is then proposed for accelerograms from the same database, aimed at simultaneously matching the requirements of two spectra (vertical and horizontal) at two vibration periods that are typically far apart. To encompass a wide range of real applications, both low-rise and medium-rise buildings on specifically designed isolation systems are considered. This results in selecting a three-dimensional signal that is coherent with both the near-fault characteristics and the structural behaviour. This approach enables comprehensive seismic response analyses, yielding statistical insights into the combined vertical and horizontal NF effects and supporting comparisons across scenarios to determine the conditions under which these effects may be either neglected or deemed critical for design. In this regard, Eurocode 8 [44, 45] suggests a distance limit of 15 km, beyond which near-source effects should not be considered in the design of strategic buildings. Other codes, such as the American ASCE/SEI 7–22 [46], define distance as a function of the fault: 15 km (or less) from the surface projection of a known active fault capable of producing Mw = 7 or larger events, or 10 km (or less) from the surface projection of a known active fault capable of ref producing events of Mw between

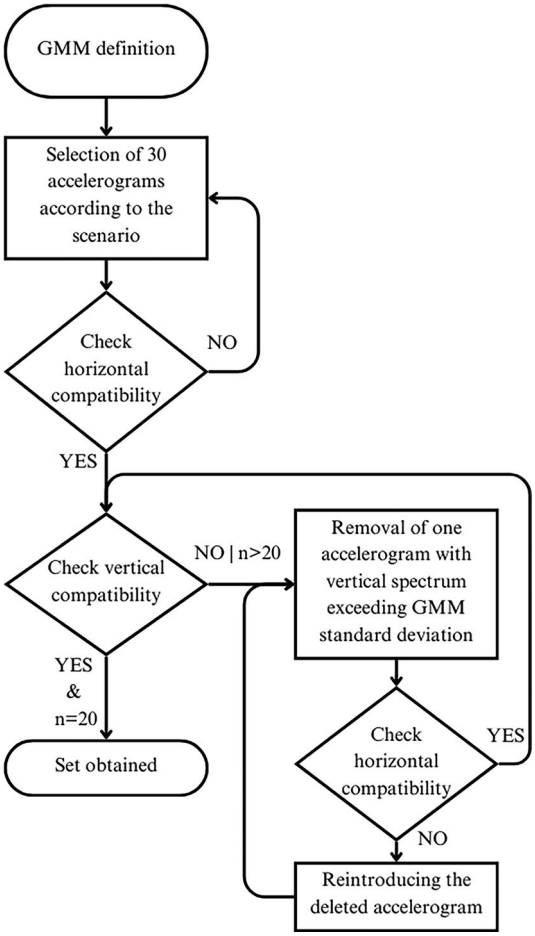

FIGURE 3 | Flow chart depicting the accelerogram selection procedure.

6 and 7. Moreover, both codes underline the importance of considering the vertical seismic component of the ground motion, especially in NF sites, for the design of base-isolated structures. The findings may contribute to the development of improved code prescriptions for designing base-isolated structures in near-fault regions.

2 | Definition of Target Spectra and Seismic Input Selection

2.1 | Background and Near-Source Scenario

The process for the site-specific record selection should provide accelerograms that are, on average, compatible with a specific target spectrum within certain tolerances, as outlined by Bommer and Acevedo [47] and Iervolino et al. [48, 49]. In this context, the use of natural accelerograms, which are recordings of ground motion from real earthquakes, is preferred over artificial or simulated ones. Natural accelerograms are considered more appropriate in terms of frequency content, duration, number of cycles, and correlation between the horizontal and vertical components of the seismic motion. Furthermore, the availability of such accelerometric data is rapidly increasing through public databases. Although this procedure follows established methods, some difficulties arise when a near-fault earthquake is considered.

The proximity of the site to the seismogenic rupture can lead to peculiar effects, such as pulse-like signals, hanging-wall amplification, tectonic fling step, extreme peaks of acceleration, etc. [11, 50]. These can significantly affect signal characteristics, producing structural responses that are very different from those of far-field earthquakes. An adequate statistical assessment for the definition of GMM models and design spectra was not possible until a few years ago due to the lack of a large set of near-fault recordings that only recently increased, thanks to the densification of the accelerometric network. To investigate the effect of near-fault earthquakes on the seismic response of base-isolated structures, a seismic scenario has been chosen. This scenario is representative of a high seismicity area located in central Italy. The region experienced a significant seismic sequence between 2016 and 2017, which also caused substantial damage related to vertical motion [12]. This region is considered one of the most seismically active areas in Europe, characterised by an extensional tectonic setting [51]. According to the most recent seismogenic zonation of Italy (ZS16 [52]), which classifies 50 area sources in Italy with uniformly distributed seismic activity, this area falls within area source #24, which is associated with a maximum earthquake magnitude Mw 7.4, representing the highest estimated recurrence magnitude for this seismogenic zone, as determined by Visini et al. [52, 53] and derived from the largest recorded earthquake magnitude in historical seismic data (Figure 1a). This estimate corresponds to a mean annual rate of occurrence computed from the frequency–magnitude distributions by Visini et al. [52] of approximately $2 \div 3 \times 10^{-4}$ year^{-1}.

The model predictions for constructing the target spectra assume a shear wave velocity (VS, 30) of 300 m/s in the upper 30 m of subsoil, representing the 'worst-case' scenario for evaluating seismic-isolated structures. Yet, given that the area is intersected by a fault system consisting of adjacent SW-dipping fault segments, the spectra for a normal faulting style have been accordingly tailored. Four distinct Joyner–Boore distances (R_{JB}), defined as the shortest distance from a site to the surface projection of the rupture plane, have been selected for the following parametric analysis: 0, 5, 15, and 30 km. Hereafter, Sections 2.2 and 2.3 describe the main features of the process utilised to define the target spectra and the set of natural accelerograms representative of near-fault earthquakes, according to the seismic scenario chosen.

2.2 | Ground Motion Model for Near-Fault Earthquakes

To address the limitations of the standard process for near-source scenarios previously described, the horizontal target spectrum has been computed using a GMM model defined in accordance with the previously selected seismic region (ITA18 [10]), modified to take into account near-fault effects [11]. This adjustment is based on an empirical correction factor derived from ITA18 residuals (ITA18-NESS) with respect to a globally sampled dataset designed for near-source effects (NESS2.0) and applied to the median predictions of the GMM. It is worth noting that the NESS2.0 is a database of waveforms from medium to strong

TABLE 1 | Selected accelerogram for R_{JB} equal to 0 km.

Record number	Record sequence	File name	Station	Mw	*RJB* (km)	Average $S_{aRotD50}$	Network code	Pulse period (s)
1	26	EMSC-20100903_0000044	GDLC	7.1	1.1	0.36	NZ	2.25
2	367	INT-UT19990920_174715	B068	7.58	0	0.46	A	11.92
3	317	EMSC-20161113_0000048	WDFS	8	4.8	0.22	NZ	—
4	110	EMSC-20140824_0000036	1765	6.07	3.3	0.24	NP	4.47
5	222	EMSC-20161113_0000048	KEKS	8	1.6	0.22	NZ	8.93
6	1087	USGS-usp0003afe	5051	6.6	0.7	0.31	M	2.39
7	50	EMSC-20110221_0000047	CCCC	6.2	3.3	0.23	NZ	—
8	1057	USGS-usp00013ee	E070	6.5	1.3	0.3	M	4.10
9	1055	USGS-usp00013ee	E050	6.5	1	0.31	M	4.06
10	1054	USGS-usp00013ee	E040	6.5	4.2	0.25	M	4.68
11	1002	USGS-us20005iis	KMM15	7	0	0.43	BO	4.26
12	1004	USGS-us20005iis	KMM10	7	0	0.21	BO	3.23
13	864	TK-1992-0002	2402	6.6	0.9	0.27	TK	2.86
14	397	INT-UT19990920_174715	B065	7.58	0	0.42	A	5.98
15	1058	USGS-usp00013ee	E080	6.5	4.6	0.17	M	5.15
16	1189	UZ-1976-0001	GZL	6.7	3.7	0.17	A	4.63
17	365	INT-UT19990920_174715	B133	7.58	0	0.25	A	7.90
18	748	IR-2003-0041	BAM	6.5	0	0.22	I1	2.01
19	42	EMSC-20100903_0000044	ROLC	7.1	0	0.23	NZ	7.14
20	223	EMSC-20161113_0000048	KIKS	8	0	0.21	NZ	5.54

global seismic events ($M \geq 5.5$) recorded near the source. This database, along with the European accelerometric database ESM (Engineering Strong Motion Database [54]), is also utilised for the record selection process. Consequently, both the target spectra and the record selection are based on the same waveform dataset. The accelerometer signals archived in these databases are all processed consistently through a manual procedure [55] and are associated with high-quality event and station metadata, which are updated periodically. Horizontal spectra are computed in terms of RotD50, i.e., the median value of spectral accelerations acting along all possible orientations, which provides a robust representation of ground motion [56]. After defining the horizontal target spectrum, the vertical target spectrum is derived from the vertical-to-horizontal response spectral amplitudes suggested by Ramadan et al. [12], which incorporates an adjustment term to improve prediction in near-source scenarios, referred to as ITA18-V(VH)-NESS. Consequently, the VH model is employed to produce vertical response spectra that are consistent with the horizontal spectra and the near-source scenario. A flow-chart of the methodology is illustrated in Figure 1b, more details are described in Sgobba et al. [57].

Figure 2a,b shows the obtained response spectra referring to Mw equal to 7.4, according to the scenario chosen for horizontal and vertical pseudo-accelerations, while Figure 2c shows the horizontal spectra in terms of displacement. In this latter figure, for comparison purposes, displacement spectra computed using the ITA18 [10] ground motion model (GMM), which does not account for near-fault effects, are shown with dashed lines, while those obtained with the ITA18-NESS [11] GMM are shown with continuous lines. As expected, a decrease in the distance from the source provides an increase in both the vertical and the horizontal spectra. Moreover, a clear peak in the 4–5 s period range can be observed for the lowest distances that may be related to the pulse period of the signal. For the distances of 15 and 30 km, this amplification disappears, confirming that the pulse-like effect is no longer important. Furthermore, Figure 2c indicates that the increased displacement demand caused by near-fault effects becomes negligible at a distance of 30 km. By observing the spectra derived from near-source GMMs, some considerations can be made for base-isolated structures at reduced distances from the fault as follows: (i) regarding the horizontal action, isolation periods should be notably shorter than 4 s to avoid excessive displacement demand at the base, and (ii) regarding the vertical action, the acceleration can exceed the acceleration due to gravity, due to the high stiffness of the isolation devices in that direction leaving the building short vertical period practically unchanged. A zoomed-in representation of the horizontal and vertical spectra around the typical horizontal and vertical isolation period ranges is reported in the corresponding pseudo-acceleration spectra.

2.3 | Seismic Input Variability and Accelerogram Selection

In the case of a near-source earthquake, vertical motion often exceeds horizontal motion at periods less than about 0.3 s,

TABLE 2 | Selected accelerogram for R_{JB} equal to 5 km.

Record number	Record sequence	File name	Station	Mw	*RJB* (km)	Average $S_{aRotD50}$	Network code	Pulse period (s)
1	1057	USGS-usp00013ee	E070	6.5	1.3	0.3	NZ	4.10
2	26	EMSC-20100903_0000044	GDLC	7.1	1.1	0.36	NZ	2.25
3	27	EMSC-20100903_0000044	HORC	7.1	7.2	0.28	M	2.60
4	1058	USGS-usp00013ee	E080	6.5	4.6	0.17	A	5.15
5	395	INT-UT19990920_174715	B076	7.58	0	0.17	NP	6.38
6	110	EMSC-20140824_0000036	1765	6.07	3.3	0.24	A	4.47
7	689	INT-UT19990920_174715	B109	7.58	7.8	0.27	A	—
8	465	INT-UT19990920_174715	B120	7.58	3.1	0.18	BO	—
9	1004	USGS-us20005iis	KMM10	7	0	0.21	NZ	3.23
10	317	EMSC-20161113_0000048	WDFS	8	4.8	0.22	BO	—
11	1005	USGS-us20005iis	KMM17	7	0.6	0.18	NZ	6.10
12	31	EMSC-20100903_0000044	LINC	7.1	5.4	0.24	CE	7.62
13	1105	USGS-usp00040t8	58065	6.9	7.6	0.15	M	4.52
14	1054	USGS-usp00013ee	E040	6.5	4.2	0.25	BO	4.68
15	1003	USGS-us20005iis	KMM16	7	2.3	0.22	A	2.96
16	660	INT-UT19990920_174715	WGK0	7.58	7.1	0.32	A	4.96
17	455	INT-UT19990920_174715	B122	7.58	2.7	0.15	A	—
18	404	INT-UT19990920_174715	B067	7.58	0	0.22	BO	—
19	837	JP-2000-0007	TTR02	6.6	1	0.18	A	1.01
20	393	INT-UT19990920_174715	B075	7.58	0	0.24	NZ	5.02

particularly within 10 km from the source and for earthquakes with magnitudes greater than 6.5, as observed by many authors (Ramadan et al. [12] among others). For this reason, the resultant spectrum of waveforms needs to align with both horizontal and vertical target spectra simultaneously (i.e., three-components compatibility), which is very hard to achieve for the entire spectral period range. For this reason, a specific procedure for the record selection is proposed hereafter, aimed at simultaneously satisfying the spectral compatibility requirement for both vertical and horizontal spectra at two different vibration periods, corresponding to the first vertical and horizontal vibration modes of the considered structure. To do this, first, a selection of a set of accelerograms larger than the final required set is made, checking the common horizontal spectrum compatibility. Then, a reduced set is considered, removing iteratively one accelerogram at each step until both vertical and horizontal compatibility is obtained on the specified subset of signals. At the first subset meeting these criteria, the procedure ends; if no subset of records fulfils the imposed conditions, the procedure is repeated with a larger pool of horizontal records, as shown in the flow chart of Figure 3. It is important to note that the period ranges of interest for horizontal and vertical seismic demands typically differ significantly, due to the substantially greater vertical stiffness of structures compared to their horizontal stiffness. Consequently, spectral matching is performed separately for the horizontal and vertical components, within distinct period ranges. In this application, base-isolation structures have been considered; thus, the period ranges selected are in the neighbourhood of the isolation period, i.e., 2–4 s for the horizontal target spectra and in the proximity of the period of the first vertical vibration mode of the whole structural system (0–0.15 s) for the vertical spectrum (see Figure 2a,b). It should be noted that seismic codes typically require spectrum compatibility over a wide range of periods to capture most of the significant structural behaviour. However, in base-isolated structures, the first vibration modes usually mobilise more than 90% of the mass. Therefore, a narrower period range is sufficient for this type of structure, as long as it covers the potential nonlinear behaviour of the isolation system. It is worth noting that this choice, together with the use of the same database for record selection as for the GMMs, greatly facilitates compatibility with both vertical and horizontal spectra, without the need to scale the records. Specifically, in this application, the target was to select 20 accelerograms with three-component compatibility, which is generally considered a statistically sufficient population for characterising the seismic response of a structure [58], and the procedure began by selecting 30 accelerograms with two-component compatibility. According to the GMM adopted, the accelerogram selection is conducted by using the RotD50 spectral acceleration intensity measure for the horizontal components. This measure also has the advantage of mitigating the dependency on a specific orientation of ground motion, leading to a more generalised and reliable assessment of seismic demand [59, 42]. In light of the above, the selection of earthquake signals has been done through the Rexelweb tool [57], by setting the following criteria, including the scenario characteristics:

TABLE 3 | Selected accelerogram for R_{JB} equal to 15 km.

Record number	Record sequence	File name	Station	Mw	*RJB* (km)	Average $S_{aRotD50}$	Network code	Pulse period (s)
1	39	EMSC-20100903_0000044	REHS	7.1	19.5	0.18	NZ	9.51
2	928	USGS-iscgem787038	VNO0	6.7	19.2	0.16	M	4.26
3	1053	USGS-usp00013ee	E030	6.5	10.1	0.15	M	5.21
4	21	EMSC-20100903_0000044	CRLZ	7.1	17.6	0.1	NZ	9.88
5	1133	USGS-usp00059sn	22074	7.3	16.3	0.1	CE	7.39
6	145	EMSC-20161030_0000029	MZ50	6.5	11.7	0.11	3A	—
7	918	USGS-iscgem787038	OHI0	6.7	17.5	0.15	M	—
8	17	EMSC-20100903_0000044	CBGS	7.1	18.1	0.16	NZ	5.94
9	1060	USGS-usp00013ee	E110	6.5	13.1	0.12	M	7.23
10	20	EMSC-20100903_0000044	CMHS	7.1	17.8	0.13	NZ	—
11	1052	USGS-usp00013ee	E020	6.5	12.6	0.1	M	5.18
12	411	INT-UT19990920_174715	C029	7.58	10.3	0.13	A	—
13	1012	USGS-us20005iis	KMM19	7	16.4	0.13	BO	—
14	16	EMSC-20100903_0000044	CACS	7.1	14.2	0.11	NZ	—
15	1119	USGS-usp00056e1	1583	7	17.2	0.12	M	—
16	346	EMSC-20190706_0000043	SRT	7.1	14.6	0.18	CI	6.71
17	1067	USGS-usp00013ee	WSM0	6.5	14.7	0.08	M	—
18	23	EMSC-20100903_0000044	DFHS	7.1	11.6	0.1	NZ	—
19	1094	USGS-usp00040t8	47381	6.9	12.6	0.11	CE	2.62
20	409	INT-UT19990920_174715	B061	7.58	10.2	0.16	A	—

i. Magnitude range, Mw: Recordings from events with magnitude 7.4 ± 1.5 are considered, consistent with the maximum earthquake scenario expected in area source #24.

ii. Epicentral distance range: Set according to the testing levels [0, 5, 15, 30] ± 5 km.

iii. Ground motion components: A three-component selection is performed in the period range 2–4 s for the horizontal components (typical range for base-isolated structures) and 0–0.15 s for the vertical ones.

iv. Tolerances of spectrum-compatibility: Set the tolerances specified by the Italian Building Code (NTC2018 [60]; paragraph 3.2.3.6) that considers a lower limit of 10% and an upper limit of 30%, in the range of periods of interest.

v. Scaling factors: No scale factors are used; this is particularly appreciable because the record scaling practice can lead to unrealistic energy content in spectra (incompatible with scenario characteristics of the site) and to inaccuracies in the nonlinear structural response [61].

In the selection procedure, no consideration is given to the focal mechanism and site conditions. The reason is that spectral matching is considered a sufficient criterion for accurate input estimation, thereby rendering it unnecessary to force that accelerograms originate from identical focal mechanisms, seismic sources, or site conditions as the target spectrum [62].

Tables 1–4 report the accelerograms chosen for the selected four distances. In the tables, the average spectrum over a specific period range is also provided for each accelerogram as the intensity measure [63, 64]. This approach facilitates the efficient identification of the average horizontal spectral acceleration ($S_{aRotD50,avg}$) for each event, providing a representative measure across all orientations and confined to the specified period range. It can be observed that the value of $S_{aRotD50,avg}$ in the range of 2–4 s period is between 0.46 × *g* and 0.17 × *g* when the distance is 0 km (Table 1), while at 30 km it assumes values between 0.15 × *g* and 0.17 × *g*. Notably, the number of recordings identified as pulse-like according to [1, 65] increases as the source-to-site distance decreases, as shown by the last columns of Table 1 through Table 4, where pulse-like periods are reported (if no value is assigned, the record is not pulse-like). This increase is a consequence of the spectral characteristics defined by the target spectrum, which is specifically tailored to account for near-source effects such as directivity pulses. As a result, the selection process inherently favours impulsive records without the need for any explicit constraints. For instance, the proportion of pulse-like records, which reaches approximately 90% at zero distance (Table 1), declines to less than 30% at R_{JB} equal to 30 km (Table 4). This decrease can be attributed to the diminished influence of the NESS adjustment at greater distances, as discussed by Sgobba et al. [11]. Overall, the selection procedure demonstrates robustness, as the inclusion of pulse-like records and, consequently, the contribution of near-source effects are implicitly and statistically well represented in the final record set.

TABLE 4 | Selected accelerogram for R_{JB} equal to 30 km.

Record number	Record sequence	File name	Station	Mw	*RJB* (km)	Average $S_{aRotD50}$	Network code	Pulse period (s)
1	461	INT-UT19990920_174715	B140	7.58	28.8	0.11	A	—
2	468	INT-UT19990920_174715	B145	7.58	31.2	0.1	A	—
3	30	EMSC-20100903_0000044	KPOC	7.1	30.3	0.1	NZ	—
4	35	EMSC-20100903_0000044	NNBS	7.1	26.8	0.15	NZ	7.56
5	1116	USGS-usp00040t8	VMP0	6.9	33.3	0.1	M	4.49
6	32	EMSC-20100903_0000044	LPCC	7.1	25.6	0.06	NZ	10.63
7	924	USGS-iscgem787038	SNS0	6.7	27.6	0.07	M	5.12
8	925	USGS-iscgem787038	SNT0	6.7	27.4	0.07	M	—
9	1114	USGS-usp00040t8	SLA0	6.9	30.2	0.11	M	3.16
10	926	USGS-iscgem787038	SST0	6.7	27.4	0.07	M	—
11	449	INT-UT19990920_174715	B113	7.58	25.8	0.1	A	—
12	1090	USGS-usp00040t8	47179	6.9	28.3	0.06	CE	—
13	1124	USGS-usp00056e1	1582	7	28.7	0.1	NP	—
14	244	EMSC-20161113_0000048	MOLS	8	26.7	0.05	NZ	—
15	480	INT-UT19990920_174715	C032	7.58	34.4	0.1	A	—
16	479	INT-UT19990920_174715	C082	7.58	34.2	0.07	A	—
17	472	INT-UT19990920_174715	C094	7.58	32.1	0.11	A	—
18	1020	USGS-us20005iis	MYZ11	7	29.8	0.04	BO	9.51
19	838	JP-2004-0002	NIG0E	6.6	25.5	0.07	BO	—
20	1185	USGS-usp00066k9	5459	6.7	28.6	0.11	NP	—

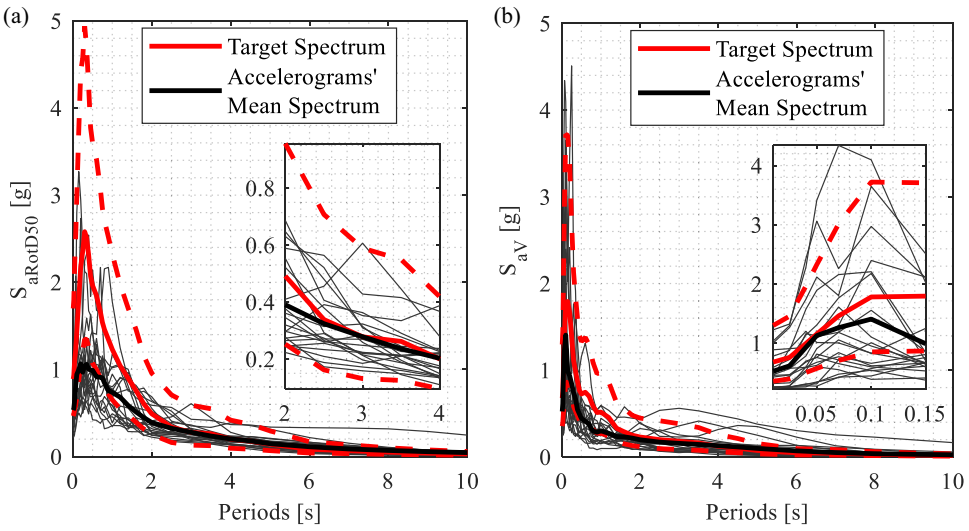

FIGURE 4 | Horizontal (a) and vertical (b) spectra of the 20 selected accelerograms for R_{JB} equal to 0 km.

Figures 4–7 depict the response spectra for the selected accelerograms, together with their mean value and the target spectrum from the adopted GMM ± one standard deviation (red dashed lines). Furthermore, zoomed-in representations of the horizontal spectra around the isolation period and the vertical spectra around the vertical period are also depicted. For the horizontal accelerograms, it is possible to highlight the alignment of the average response spectrum with the target spectrum, while the spectra of the individual accelerograms fall within the standard deviation of the used GMM. With regard to the vertical component, priority is given to verifying that the mean spectrum of the accelerograms is close to the target spectrum (within the range of periods of interest, namely 0–0.15 s), while it is accepted that a few accelerograms exceed the standard deviation.

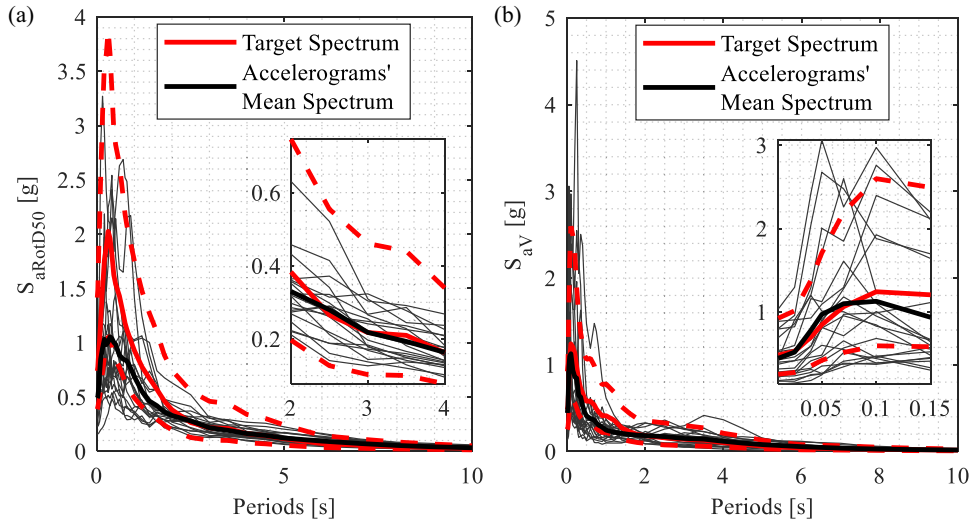

FIGURE 5 | Horizontal (a) and vertical (b) spectra of the 20 selected accelerograms for R_{JB} equal to 5 km.

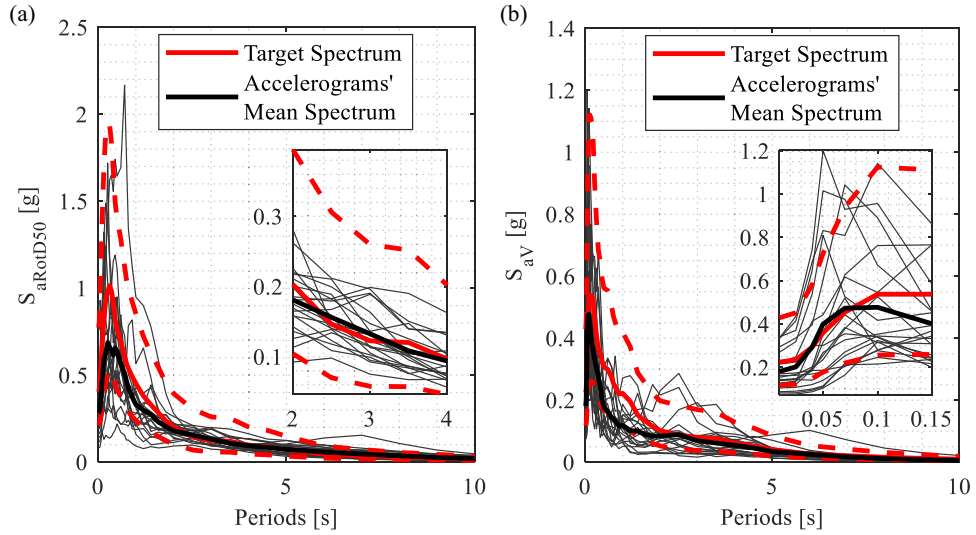

FIGURE 6 | Horizontal (a) and vertical (b) spectra of the 20 selected accelerograms for R_{JB} equal to 15 km.

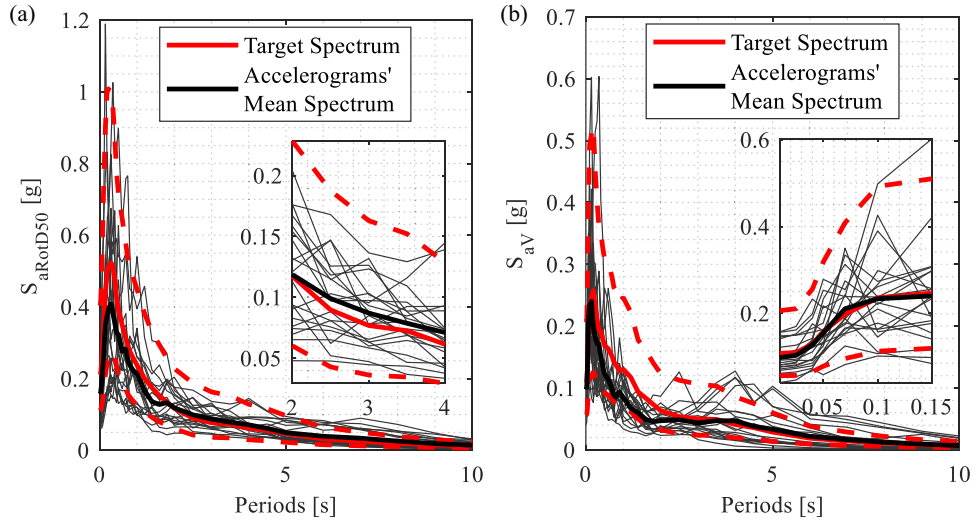

FIGURE 7 | Horizontal (a) and vertical (b) spectra of the 20 selected accelerograms for R_{JB} equal to 30 km.

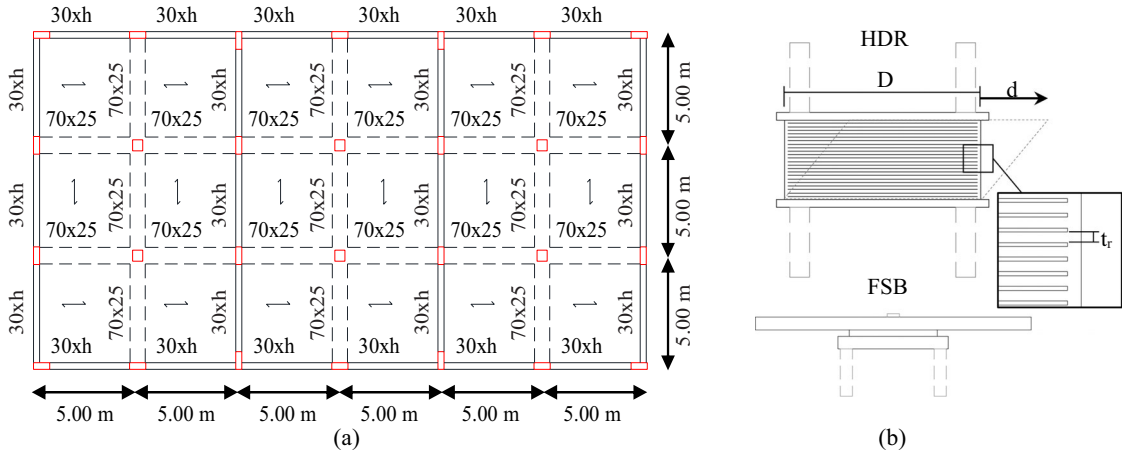

FIGURE 8 | Plan view of case studies (a) and schematic drawing of HDRBs (b).

TABLE 5 | Section dimensions of beams and columns for three-storey superstructure.

Floor	Beams (cm)	Columns (cm)	
		Rectangular	Square
1	40 × 30	40 × 30	40 × 40
2	40 × 30	40 × 30	40 × 40
3	40 × 30	40 × 30	40 × 40

TABLE 6 | Section dimensions of beams and columns for nine-storey superstructure.

Floor	Beams (cm)	Columns (cm)	
		Rectangular	Square
1–3	60 × 30	80 × 30	50 × 50
4–6	50 × 30	60 × 30	45 × 45
7–9	40 × 30	40 × 30	40 × 40

3 | Base-Isolated Case Studies

This paper assesses NF effects for base-isolated buildings subjected to near-source scenarios, as outlined in Section 2. Two archetype structures, i.e., a three-storey and a nine-storey building, are considered, as detailed in Section 3.1. Section 3.2 describes the base-isolation systems employed at varying distances from the fault, while Section 3.3 presents the numerical modelling approach used for the complete base-isolated structural systems.

3.1 | Case Studies Description

In this research, two structures with different dynamic characteristics have been evaluated. Specifically, three-dimensional base-isolated reinforced concrete (RC) structures with three and nine storeys have been selected as reference case studies. The structural plan, common to both the archetypes, has a rectangular shape of 30 m × 15 m. The inter-storey height is equal to 3.2 m, while the span length is 5 m in both directions. The structures have six and three spans in the principal directions. The structural system of the buildings consists of a reinforced concrete frame structure decoupled from the ground by means of a base isolation system. A plan view of case studies is illustrated in Figure 8a, while in Figure 8b a schematic drawing of isolation devices is reported. In Tables 5 and 6, the section dimensions of beams and columns are reported, while in Table 7, periods of the fixed base structure are summarised.

3.2 | Base-Isolation Systems and Superstructure Design

This study considers rubber-based isolation systems, either using HDRBs only or in combination with low-friction flat sliding bearings (FSBs) (see Figure 8b). The combination of HDRBs and FSBs in base isolation systems, commonly referred to as hybrid isolation systems, enables longer isolation periods compared to solutions employing HDRBs alone. Specifically, for a given isolator size, the total number of isolators can be reduced by strategically placing low-friction sliders beneath selected columns. These components provide vertical load-bearing capacity without significantly contributing to the horizontal stiffness of the isolation system, thereby optimising the isolation period. The primary objective of the design is to optimise the isolation system for the different scenarios. More in detail, the design of the rubber-based isolation system is ruled by the choice of the following three parameters: the diameter of the rubber bearing D, the total height of the rubber layers H_r, and the ratio between the number of FSBs and the total number of devices. The following design criteria are required to be satisfied: (i) the maximum shear strain $\varepsilon_{q,max}$ of HDRBs must be lower than 2.5 (which is the maximum value allowed by the code EN 15129 [66]), where $\varepsilon_{q,max}$ is the ratio between the horizontal displacement (d) and the total rubber height (H_r), (ii) the stability conditions set out in EN15129 [66] must be met, that is, the pairs σ–δ must fall within the safe domain (where σ is the mean vertical stress on a single HDRB, δ is the horizontal displacement normalized with respect the bearing diameter), (iii) the shape factors of HDRBs must remain within

TABLE 7 | Modal characteristics of the superstructure considered as fixed base.

Direction	Three-storey periods (s)	Nine-storey periods (s)
X	0.30	0.82
Y	0.10	0.14
Z	0.06	0.11

TABLE 8 | Summary table of the design results for the three-storey superstructure.

R_{JB} (km)	n HDRB (-)	n FSB (-)	D (mm)	H_r (mm)	V (mm^3)	P_{cr} (kN)	d_{cav} (mm)	S_2 (-)	T_{iso} (s)	Acronym
0	12	16	928	253	1.71E+08	22820	0.04	3.67	2.5	3 St,0R_{JB}
5	14	14	766	200	9.18E+07	16212	0.03	3.84	2.5	3 St,5R_{JB}
15	22	6	489	132	2.48E+07	6435	0.02	3.70	2.5	3 St,15R_{JB}
30	26	2	355	81	8.03E+06	3910	0.01	4.39	2.5	3 St,30R_{JB}

a commercial range, in particular the second shape factor S_2, defined as the ratio D/H_r, must be larger than 3.5, while the first shape factor $S_1 = D/(4t_r)$ (where t_r is the thickness of a single rubber layer, as depicted in Figure 8b) is set almost equal to 20 according to common values used by the European manufacturer (to ensure a vertical stiffness much larger the horizontal one), (iv) the isolation period T_{ISO} is higher than three times the first horizontal period of the fixed-base superstructure (T_{FBSS}), and $T_{ISO} > 2$ s to be appropriate for the isolation and (v) the tensile strength of the HDRBs must be lower than the design limits for cavitation according to EN15129 [66] indications (i.e., $\sigma_y = 2G$). The properties variability of HDRBs is also accounted for, again according to European practice (EN15129 [66]). Specifically, the preliminary design of the bearings is performed through linear dynamic analysis using displacement response spectra (illustrated in Section 2.2 for the different scenarios but amplified by a factor of 1.2 to convert from RotD50 to RotD100) and nominal equivalent linear parameters for HDRBs (G = 0.4 MPa and $\xi = 15\%$). According to EN15129, nominal HDRB parameters refer to values obtained at the third cycle of 100% shear strain under non-aged conditions at a reference temperature of 23°C. Thus, to account for production variability, lower bound (LB) properties are derived by multiplying nominal values by 0.8, as indicated in Table 4 of Micozzi et al. [67], and used to design the isolation system. It should be noted that this procedure, based on third-cycle data, is appropriate for short-duration ground motions, but may not be entirely accurate for long-duration ground motions [68], which, however, are very rare in the European context. Finally, the friction of sliders has been neglected in the design procedure, due to the very low value (imposed lower than 1%).

For the cases where the obtained number of HDRBs is lower than the number of columns, FSBs are used in combination with HDRBs, resulting in hybrid systems. In this case, HDRBs are placed along the perimeter of a building to maximise the torsional stiffness of the isolating system. In contrast, the FSBs are placed under the central area of the building and are designed mainly with reference to the maximum vertical load sustained. The values of the parameters resulting from the optimised design are summarised in Tables 8 and 9 for the superstructures with three and nine storeys, respectively. Figure 9 shows a schematic overview of the in-plane position of HDRBs and FSBs. It should be specified that the number of sliding bearings represents the minimum required to achieve the target isolation period, set to 2.5 and 3.5 s for the three- and nine-story cases, respectively.

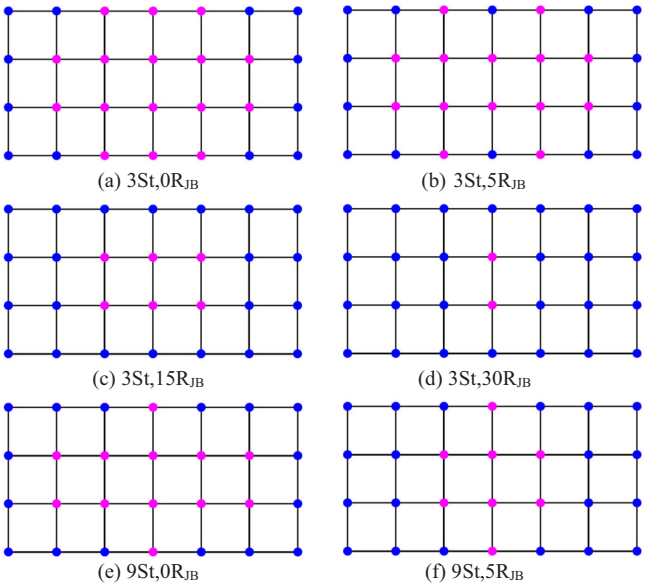

FIGURE 9 | HDRBs (blue dots) and FSBs (magenta dots) position scheme.

As shown in the tables, the number of bearings decreases with increasing distance from the fault in both cases. This is because the design of the isolators is governed by the condition $\delta < 0.7$ (i.e., bearing diameter larger than 70% of the displacement demand), imposed by the stability domains of EN15129 [66], leading to increasingly larger HDRB diameters. Consequently, as the distance from the fault decreases, the bearings' stiffness increases, so their number must be reduced to maintain the total system stiffness. As reported in the same tables, the critical load in the undeformed configuration (P_{cr}) also increases. As a result,

TABLE 9 | Summary table of the design results for the nine-storey superstructure.

R_{JB} (km)	n HDRB (-)	n FSB (-)	D (mm)	H_r (mm)	V (mm^3)	P_{cr} (kN)	d_{cav} (mm)	S_2 (-)	T_{iso} (s)	Acronym
0	16	12	1136	308	3.12E+08	34553	0.04	3.69	3.5	9 St,0R_{JB}
5	20	8	875	231	1.39E+08	20645	0.03	3.79	3.5	9 St,5R_{JB}
15	28	0	663	179	6.16E+07	11391	0.03	3.71	3.5	9 St,15R_{JB}
30	28	0	467	90	1.54E+07	7860	0.01	5.19	3.5	9 St,30R_{JB}

only the nine-story structure cases at 15 and 30 km are designed with HDRBs without sliders. In the latter case, a reduction in shear strain with respect to the target value is adopted to increase the secondary shape factor S_2 and consequently the critical load, as shown later in the paper in the stability domains. A further remark is about the variation of the vertical stiffness of HDRBs in the deformed configuration that could potentially lead to a compatibility issue between the vertical displacements of HDRBs and FSBs [69]. The adopted design choices, namely a large S_1 value and an S_2 value satisfying the condition $\delta < 0.7$, ensure a minimal vertical displacement for HDRBs during the horizontal motion with negligible effects for the framing system.

Conversely, the superstructure has been designed by using pseudo-acceleration response spectra of Section 2.2 and by considering the upper bound (UB) properties of HDRBs. In particular, according to EN15129 [66], the production variability and the stiffening effects due to low temperatures and ageing have been considered. Modification factors equal to 1.61 for G and 1.09 for ξ have been applied to nominal values, as reported and explained in Table 4 of EN15129 [66]. However, as also emphasised in Micozzi et al. [67], it should be observed that the European standard does not consider the effect of repeated cycles (or scragging), which can lead to a significant increase in the stiffness of the isolators. As specified in Micozzi et al. [67], this effect should be taken into account when designing the superstructure, and indicative modification factors are 2.1 for G and 0.86 for ξ (leading to the maximum demand on the superstructure). Nevertheless, it should also be observed that this effect strongly depends on the rubber compound and can be even more pronounced, such as in cases involving large shear strains or large-diameter bearings [38]. Eurocodes requirements are also considered for vertical, wind, and seismic loads. More specifically, design related to wind and vertical loads follows the provisions of EN 1991-1-4 [70] and EN 1992-1-1 [71], while seismic design is carried out according to EN 1998-1 [44]. A fixed-base configuration is adopted for non-seismic load combinations, whereas for seismic combinations, HDRBs are modelled as linear elements using UB properties and considering the worst-case seismic scenario. A commercial software, SAP2000 [72], is used for the structural design. The cross-sections of the structural members are sized based on the most demanding load combination, either vertical loads combined with wind loads or vertical loads combined with seismic action, and by imposing, as concerns the seismic action, drifts lower than 0.005h (where h is the inter-storey height). The concrete strength class adopted for the study is C25/30, while the reinforcing steel is of grade B450C, with bar diameters ranging from 16 to 20 mm. Finally, the reinforcement bars are designed to ensure the elastic behaviour of the superstructure. Based on

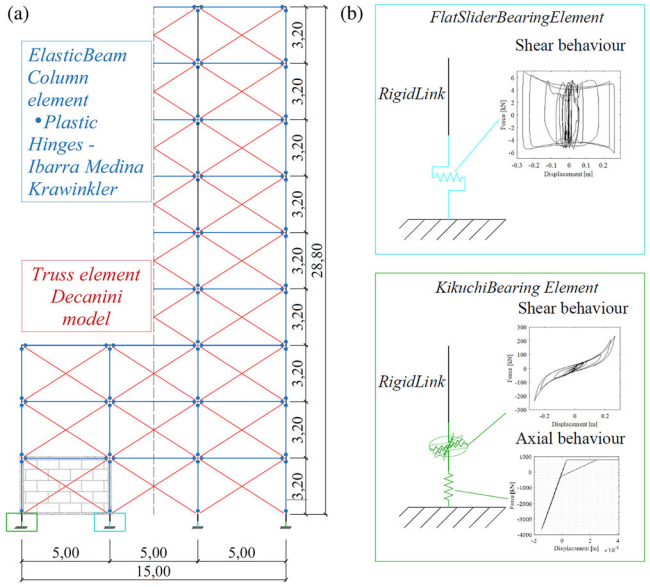

FIGURE 10 | Numerical modelling: external frame elevation.

previous observations regarding the effect of repeated cycles, it should be noted that the amount of reinforcement may be slightly underestimated. However, in this study, that effect is not considered either in the design or in the analyses, as it is not the focus of the paper.

3.3 | Numerical Modelling

The OpenSees software [73] is selected to define and investigate the numerical models of the case studies. Figure 10a depicts the numerical model of a generic frame, whereas Figure 10b illustrates the model used for FDB and HDRBs. Concerning HDRBs, they are modelled in OpenSees using the *KikuchiBearing Element* [74]. This model is one of the few existing models that can predict the complex, coupled horizontal–vertical behaviour of rubber bearings up to collapse, incorporating the influence of axial load on the horizontal behaviour and other geometric nonlinearities, such as the vertical displacement of bearings due to the horizontal deformation. It is a fully three-dimensional model for rubber bearings, where the behaviour in large displacement of the isolator is divided into a combination of the Euler column buckling behaviour and the pure shear column deformation behaviour [75, 76]. According to the large displacement formulation of the element, the force-equilibrium condition of this model considers the geometrical relationship arising among the deformation, the force equilibrium, and the P–Δ effects in the definition of

TABLE 10 | *KikuchiAikenHDR* parameters (model is in N-m-s).

Rubber type		X0.4-0MPa
Correction coefficients for equivalent shear modulus	c_g	1.15
Correction coefficients for equivalent viscous damping ratio	c_h	0.75
Correction coefficients for the ratio of shear force at zero displacement	c_u	0.75

the stiffness matrix. More in detail, the *KikuchiBearing Element* is based on two different uniaxial materials for the multiple horizontal and vertical springs. The *KikuchiAikenHDR* material is used for the horizontal behaviour [77], which has been calibrated based on third-cycle data of a large set of experimental tests [42, 41] by using the set of correction coefficients reported in Table 10. In the vertical direction, the *AxialSP* material has been adopted, with a cavitation tension limit of 2G and a post-cavitation stiffness equal to 0.43% of the initial vertical stiffness of the bearing (Figure 10b). However, differently from the original model, where this material has been used for internal multi-normal springs (MNS) in the axial direction, the material has been assigned to an external element (placed in series) while the internal axial springs are set to be elastic. This modelling solution, already adopted in a previous study [41], has been developed as the original model was found to significantly overestimate *P–Δ* effects under large deformations and compressive loads in European HDRBs (characterised by lower shear factors compared to the Japanese ones). A detailed explanation of this aspect can be found in Micozzi et al. [42]. Globally, this model is a good compromise between robustness, capability to correctly predict the coupled horizontal–vertical behaviour in compression and the cavitation in tension. To give an idea of the displacements involved, vertical displacements corresponding to the cavitation limit are reported in Tables 8 and 9 for the different isolators. The only limitation of the model is that it does not incorporate full-load history dependence, so it does not account for the repeated-cycle effect. Only a few models can do this [32–34], and only very recently have been implemented in a nonlinear three-dimensional formulation [37].

As concerns FBSs, they have been modelled by means of the *FlatSliderBearingElement*, considering a Velocity and Normal Force Dependent Friction, as defined in [78]. The sliders' breakaway has also been considered, based on Quaglini et al. [79]. The main parameters are reported in Table 11.

For the superstructures, a non-linear lumped-plasticity model has been implemented in OpenSees, as already done in [80–83]. All RC members, including the base floor grid beams above the isolation system, have been modelled as elasticBeamColumn elements with flexural plastic hinges at their ends via *zeroLength* elements. The model selected to describe the flexural behaviour of the cross-sections is the well-known Ibarra model [84, 85], implemented in OpenSees as *modIMKmodel*. The stiffer zones representative of the beam–column joints have been modelled by means *of elasticBeamColumn* elements characterised by an elastic modulus of the concrete having a higher order of magnitude with respect to the elastic modulus used for beams and columns. The

TABLE 11 | FSB *FlatSliderBearingElement* parameters (model is in N-m-s).

Constant for the coefficient of friction at low velocity	a_{slow}	0.5062
Exponent for the coefficient of friction at low velocity	n_{slow}	0.65
Constant for the coefficient of friction at high velocity	a_{fast}	0.6187
Exponent for the coefficient of friction at high velocity	n_{fast}	0.65
Constant rate parameter coefficient	α_0	18
Linear rate parameter coefficient	α_1	0
Quadratic rate parameter coefficient	α_2	0

Ibarra model can describe the post-peak degradation response, but it neglects biaxial bending and axial force interaction. Further details regarding the *modIMKmodel* can be found in [83]. The *P–Δ* effects are considered in the columns. Moreover, since the superstructure is newly designed and therefore code-compliant, the shear failures of the members as well as the inelastic response of the beam–column joints are not expected, nor modelled, while they are evaluated ex-post. Concerning the elastic stiffness of beams and columns, according to NTC 2018 [60], the cracked stiffness of the elements has been modelled by considering a reduction coefficient ranging between 0.5 and 0.8, depending on the vertical pressure ratio, consistent with the elastic behaviour of the superstructure up to very high seismic intensities. The uncracked stiffness has been taken equal to the secant modulus of elasticity of concrete E_{cm}, associated with a strength class C25/30. Furthermore, the floor rigid diaphragm of the slabs is modelled by means of truss elements, dimensioned to provide an equivalent in-plane stiffness. The contribution of masonry infill panels is also modelled in OpenSees using an equivalent compression-only strut, implemented as truss elements with uniaxial material *Concrete01*. The typology of infills refers to masonry partitions realised with hollow clay blocks having a percentage of holes ranging between 45% and 55% (strong infills according to Decanini et al. [86]). The blocks have a thickness of 30 cm, and their contribution in terms of stiffness is notable. The skeleton curve of the diagonal strut has been derived according to a modified version [87] of the original Decanini model [86]. The effects of the openings have been considered through suitable reduction factors [88]. The resulting *Concrete01* parameters are compressive strength of 215 kN at the first floor and 500 kN at all the other floors, strain at maximum stress of 0.1% and the strain at crushing stress of 0.8%. The viscous damping related to the elastic response of the superstructure has been modelled by applying the stiffness-proportional damping matrix to only the elastic element members (beam and column elements) of the superstructure. The coefficient has been calibrated to provide an equivalent damping ratio $\xi = 2\%$ at the first modal frequency in a fixed-base configuration (see Table 7). The equivalent damping ratio is limited to 2% to avoid suppression of higher modes' response. This strategy is one of the possible solutions to avoid the so-called 'damping leakage' and to obtain a reasonable behaviour of the superstructure without altering the seismic isolation response [89–91].

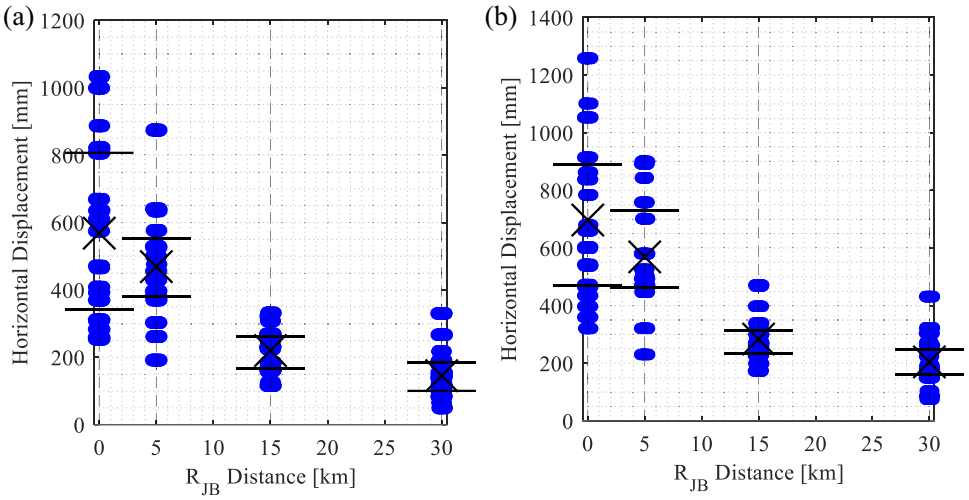

FIGURE 11 | Maximum horizontal displacement for: (a) three-storey and (b) nine-storey superstructures.

4 | Seismic Analyses Results Under the Selected Scenarios

This paragraph presents the outcomes of the nonlinear analyses carried out on the previously described case studies. Results are presented first in terms of maximum horizontal displacements and then in terms of maximum vertical displacements, which may lead to tensile forces in HDRBs and/or uplift on sliders. Then, axial forces and buckling stability of HDRBs are reported. Finally, the behaviour of the superstructure is shown through global structural parameters.

4.1 | Verification of HDRB Dimensions

To comprehensively describe and assess the behaviour of the isolation system, the maximum horizontal displacement has to be analysed. Figure 11 shows the maximum horizontal displacements at the ground level for each HDRB and FSB and for each accelerogram (i.e., 28 devices and 20 accelerograms resulting in a total of 560 markers for each distance), plotted against the distance from the fault. The data are presented using a swarm chart, a graphical method that displays individual data points along the *y*-axis while spreading them along the *x*-axis to prevent overlap. This visualisation technique is particularly effective for assessing the density, dispersion and, clustering of values within a dataset. In the case of Figure 11, the swarm chart clearly illustrates that, in the presence of a rigid diaphragm, the maximum horizontal displacement of each device under a given accelerogram is identical, and therefore, the data points cluster along the *y*-axis. Thus, their dispersion along the *y*-axis represents record-to-record variability, the X marker indicates the mean across the 20 time histories, and the horizontal lines represent the first and third quartiles. As can be seen, the displacement demand increases significantly as the distance from the fault decreases, as does the associated dispersion. As already mentioned, this entails the use of progressively taller and wider devices as proximity to the fault line increases. However, the displacement demand remains limited, and the isolation system remains feasible, since the target isolation periods are assumed to be shorter than the range of pulse periods discussed in Section 2.2. The average shear strains (obtained by dividing values indicated by the X by the height of the bearings) are approximately: 2.3, 2.4, 1.7, and 1.8 for the three-storey case and 2.3, 2.5, 1.6, and 2.1 for the nine-storey case, corresponding respectively to distances from $R_{JB} = 0$ km to $R_{JB} = 30$ km. Furthermore, the maximum shear strains obtained remain below the failure limit (between 350% and 400%), as they are limited by the rubber's hardening behaviour (see Figure 10b). In Figures 12 and 13, the stability domains are illustrated, giving the buckling load normalised with respect to the critical load at zero displacement (P_{cr}), as a function of the horizontal displacement normalised with respect to the bearing diameter (δ). As already mentioned, the domain is such that if the buckling load is lower than a quarter of the buckling load at zero displacement, the stability condition is governed by the maximum displacement requirement provided by the expression $\delta \leq 0.7$. Here, for clarity of data points, only the mean demand across all accelerograms for each HDRB is plotted so that the number of points corresponds to the number of HDRBs. The stability of bearings has been evaluated under two distinct conditions: the former refers to the maximum displacement, and the latter to the maximum axial force, with the corresponding axial force and displacement, respectively. Results indicate that for distances of 0, 5 and 15 km from the fault, the most unfavourable outcomes refer to the maximum displacement condition, while for distances from the fault of 30 km, all the demand points approach the inclined part of the stability domain, meaning that the combined effect of both displacements and axial compression forces becomes critical for both the demand scenarios. In general, the outcomes of three-storey and nine-storey buildings are similar. In the same figures, red points refer to the condition without the vertical seismic component. It should be noted that this component does not affect the maximum displacement demand at all, since the stability domains ensure that the bearing behaviour remains far from softening phenomena due to *P–Δ* effects. Conversely, maximum axial compression forces are affected. However, where the differences are more significant (i.e., at short distances from the fault), the points still remain well within the stability domains due to the high value of the critical load (P_{cr}). Differently, at larger distances, P_{cr} is lower, but the differences in axial forces are also smaller, so again all points remain within the stability domain. Therefore, in terms of stability and shear strain, it can be

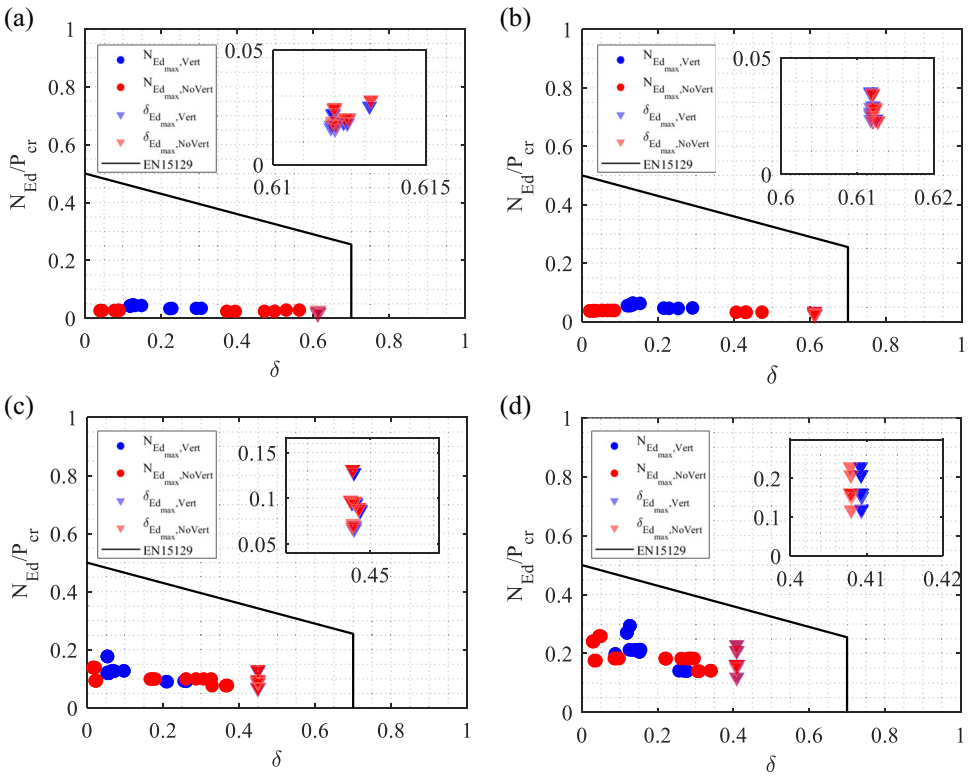

FIGURE 12 | Three storeys – design domain at R_{JB} equal to: (a) 0 km, (b) 5 km, (c) 15 km, and (d) 30 km.

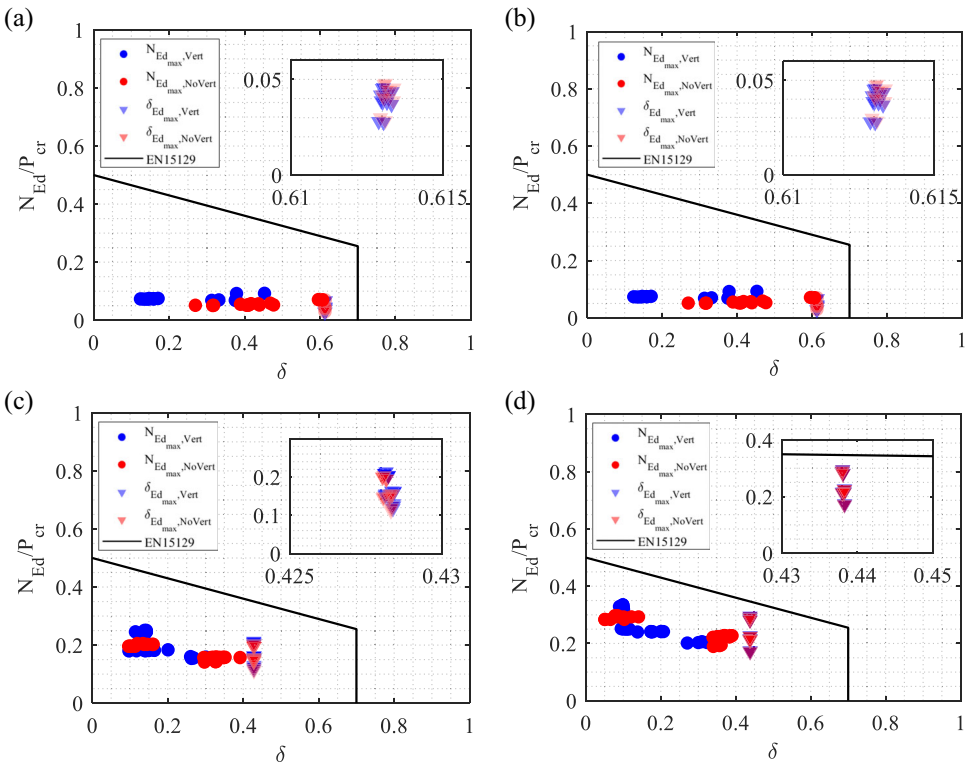

FIGURE 13 | Nine storeys – design domain at R_{JB} equal to: (a) 0 km, (b) 5 km, (c) 15 km, and (d) 30 km.

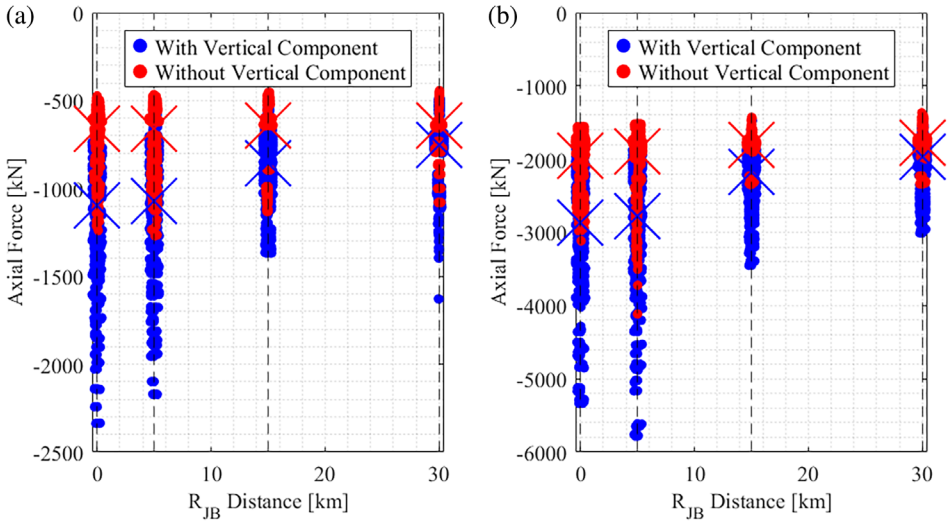

FIGURE 14 | Maximum axial force for: (a) three-storey and (b) nine-storey superstructures.

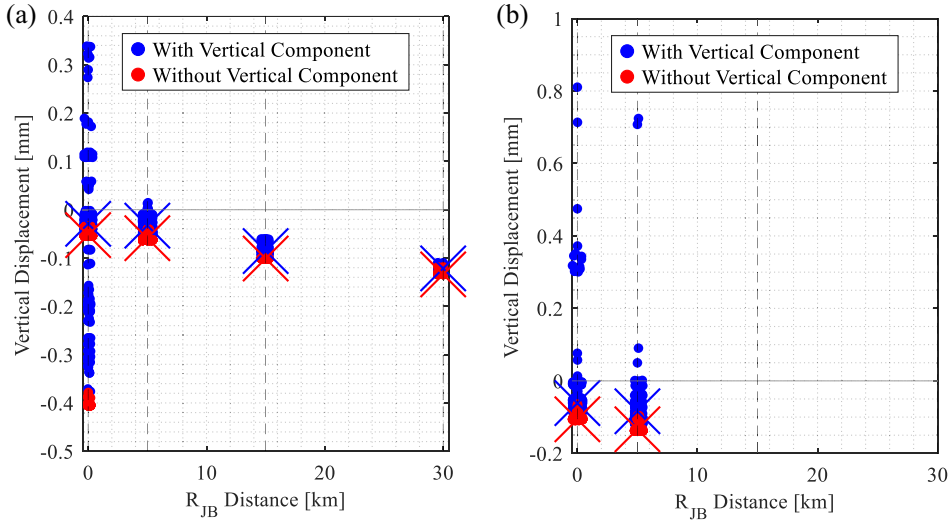

FIGURE 15 | Maximum FSB vertical displacement for: (a) three-storey and (b) nine-storey superstructures (for distances larger than 5 km, no sliders are adopted in the isolation systems).

concluded that the results are not affected by the vertical seismic input. However, a remark should be made regarding the design strategy, as the obtained results highlight the limitations of the adopted isolation system at short distances from the fault. In such cases, as in high-seismicity areas, the isolation system becomes very demanding in terms of the size of HDRBs and the number of large sliders. A greater energy dissipation capacity (e.g., through supplemental damping) would allow for smaller bearings (thus optimised also with respect to axial forces) and a reduced number of smaller sliders. However, it should be noted that the results in terms of cavitation and uplift, shown in the next section, would not improve and may even worsen.

4.2 | Vertical Displacements and Axial Forces of HDRBs and FSBs

For better assessing the impact of the vertical component, Figures 14–16 present the comparison between the results obtained from two sets of analyses, i.e., with (blue) and without (red) the vertical component of the seismic records, in terms of axial forces of both FSBs and HDRBs (Figure 14), vertical displacements for FSBs (Figure 15) and HDRBs (Figure 16) for all the devices and all records. X markers indicate the mean values (across the 20 time histories and all devices). Regarding the maximum axial force, it is evident that the discrepancy in peak values diminishes with increasing distance from the fault, indicating that the vertical component plays a more significant role in the proximity of the fault. For $R_{JB} = 30$ km, the average increment of the axial forces of the isolators is about 10% in both the three- and nine-storey buildings; differently, for RJB = 0 km and RJB = 5 km, the axial force in the presence of the vertical component is more than twice the value obtained when it is not considered. However, as already shown, this increase is not critical for the design of the isolation system. Regarding vertical displacements, the absence of uplift (positive displacements) for the FSBs was identified in analyses conducted without the vertical component, as illustrated

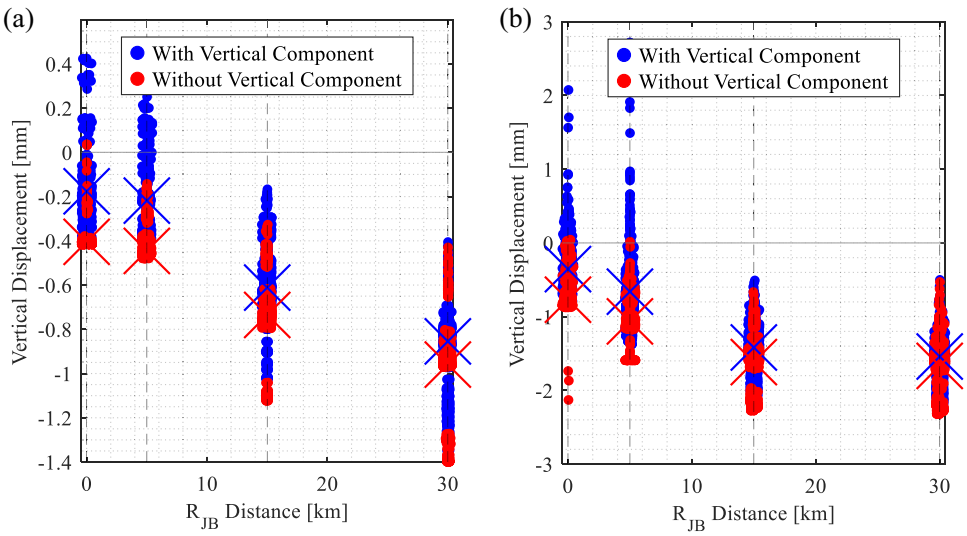

FIGURE 16 | Maximum HDRB vertical displacement for: (a) three-storey and (b) nine-storey superstructures.

in Figure 15, for both case studies and all distances from the fault. In contrast, performing numerical analyses with the vertical seismic component, uplifts are significant for $R_{JB} = 0$ km (three- and nine-storey cases) and $R_{JB} = 5$ km (only nine-storey case). Regarding HDRBs, Figure 16 demonstrates that, without the vertical seismic component, positive displacements are very low and never exceed the cavitation threshold; differently, with the vertical seismic component, HDRBs of the three-storey building at $R_{JB} = 0$ km experience positive displacements slightly larger than the cavitation limit (reported in Table 8). For the nine-storey building (at $R_{JB} = 0$ km and $R_{JB} = 5$ km), positive displacements become significantly larger than cavitation limits (reported in Table 9), due to the combined effects of the vertical seismic input and the rocking response induced by the horizontal one. To better illustrate these results, Tables 12 and 13 report the number of devices that exhibited cavitation or uplift, along with the corresponding number of records. It can be observed that cavitation and uplift occur frequently at distances of $R_{jb} = 0$ km and $R_{jb} = 5$ km. However, displacements remain within acceptable ranges: in the order of tenths of a millimetre for the sliders, and in the order of millimetres for the HDRBs (which are below the displacement failure limit in tension, as defined in Kumar et al. [26]).

4.3 | Superstructure

Concerning the superstructure, key parameters for assessing seismic performance with the vertical component of the earthquakes include the inter-storey drift ratio (IDR) and both horizontal and vertical floor accelerations. It is specified that vertical floor accelerations are measured above the columns; therefore, the potential implications of flexible slabs are not considered in this study. Figure 17 shows the IDR peak values of each accelerogram for the various distances. Here again, X marker indicates the mean value among the 20 time histories, while the horizontal lines represent the first and third quartiles. The measured mean values are less than 0.07% for the three-storey structure and 0.15% for the nine-storey structure, highlighting the effectiveness of the base isolation system in maintaining the superstructure response within the linear elastic range across all analyses (including infill panels). Figure 18 shows the peak residual inter-storey drift ratio (RIDR). Regardless of the distance, the RIDR is always significantly lower than 0.2% and 0.5%, which were identified as the thresholds for which there is no need for structural realignment and for structural repairability, respectively [92, 93]. As expected, there is no difference in these response parameters with and without the vertical seismic component because, as already mentioned, it does not influence the horizontal behaviour of HDRBs. Also, horizontal floor accelerations are very few affected by the vertical seismic component, as shown in Figure 19. Differently, it causes significant vertical floor accelerations, which are practically absent without the vertical component (due to very limited rocking effects on the structural system) and very high in its presence, especially for low distances and for the nine-storey building (Figure 20). Finally, to better assess the vertical behaviour of the superstructure, the acceleration amplification of the earthquake is computed. As illustrated in Figure 21, the maximum ratio between the peak floor acceleration (pfa) and the peak ground acceleration (pga) in the vertical direction among all the floors is reported for each record and distance. Notably, the mean value of the ratio for the three-storey structure is consistently lower than unity, thus indicating the structure's capacity to attenuate the vertical component. In the case of the nine-storey building, the mean value of the ratio approaches unity for considerable distances and slightly exceeds unity for smaller distances. This aspect should not be neglected, as it could compromise the stability of structural and non-structural elements of the superstructure.

5 | Conclusions

This paper provides a systematic approach to evaluate near-fault effects (influencing both horizontal and vertical seismic demand) by selecting appropriate near-source scenarios and recently defined near-source ground motion models (GMMs). A procedure for selecting three-component accelerograms has also been developed, using the same database as the GMMs (NESS2.0), thus ensuring compatibility with both vertical and

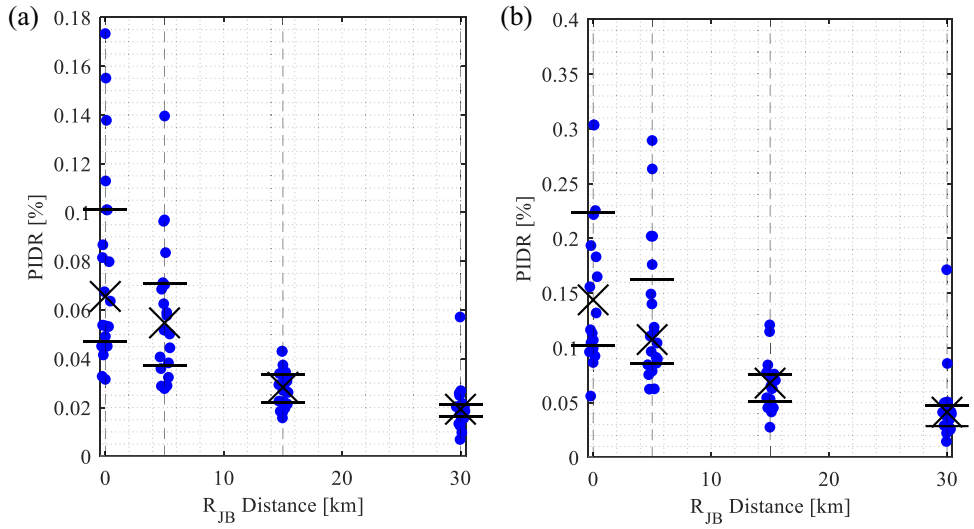

FIGURE 17 | Peak interstorey drift ratio among the floors for: (a) three-storey and (b) nine-storey superstructures.

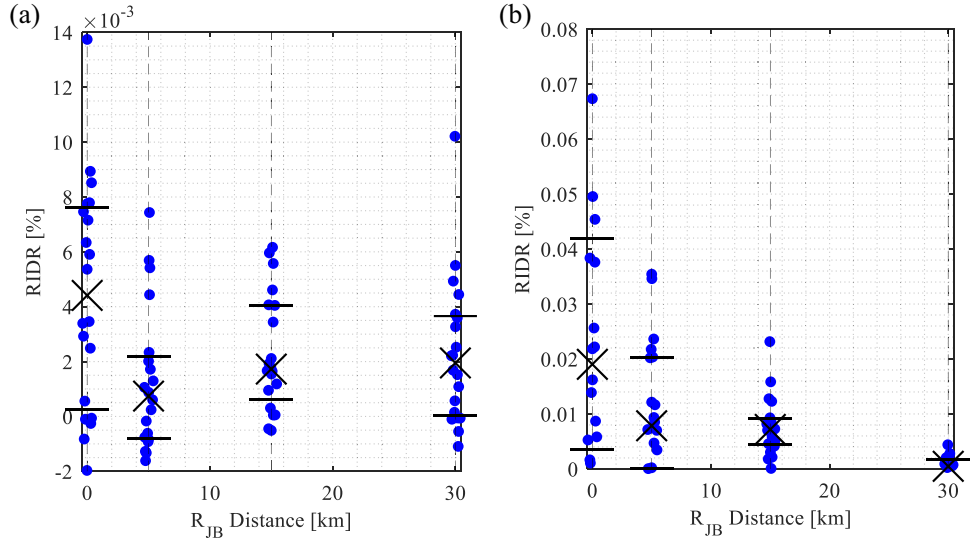

FIGURE 18 | Residual interstorey drift ratio among the floors for: (a) three-storey and (b) nine-storey superstructures.

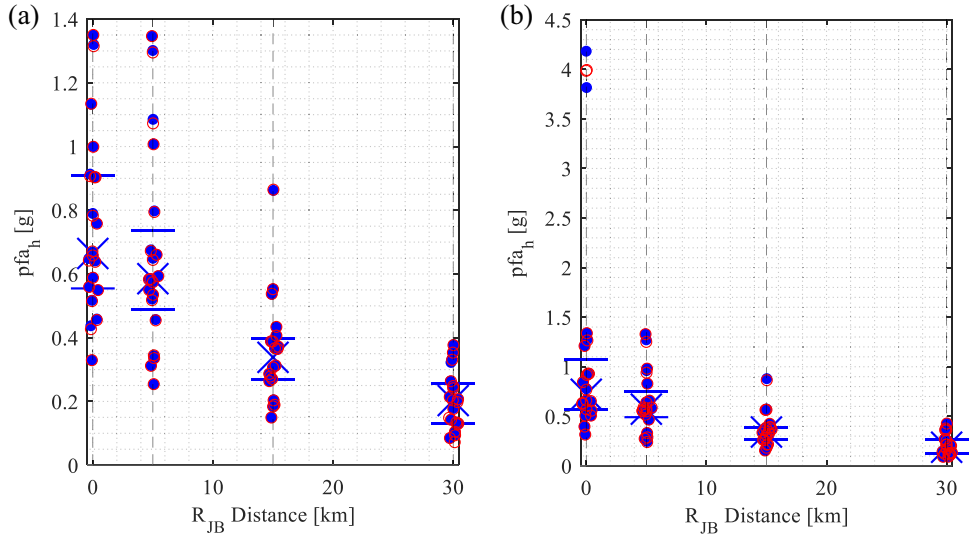

FIGURE 19 | Peak floor acceleration in horizontal direction for: (a) three-storey and (b) nine-storey superstructures. Results are reported with (filled dots) and without (empty dots) inputting the vertical component of the records.

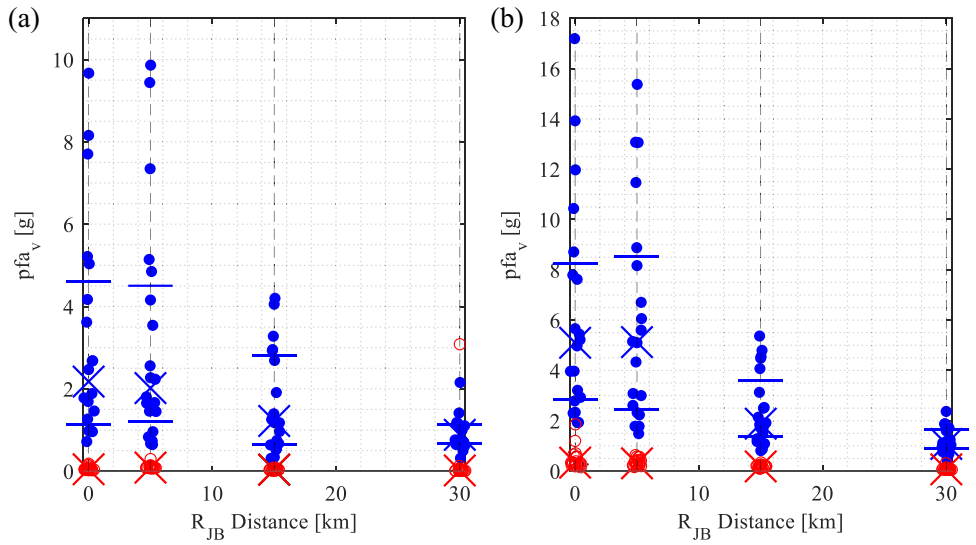

FIGURE 20 | Peak floor acceleration in vertical direction for: (a) three-storey and (b) nine-storey superstructures.

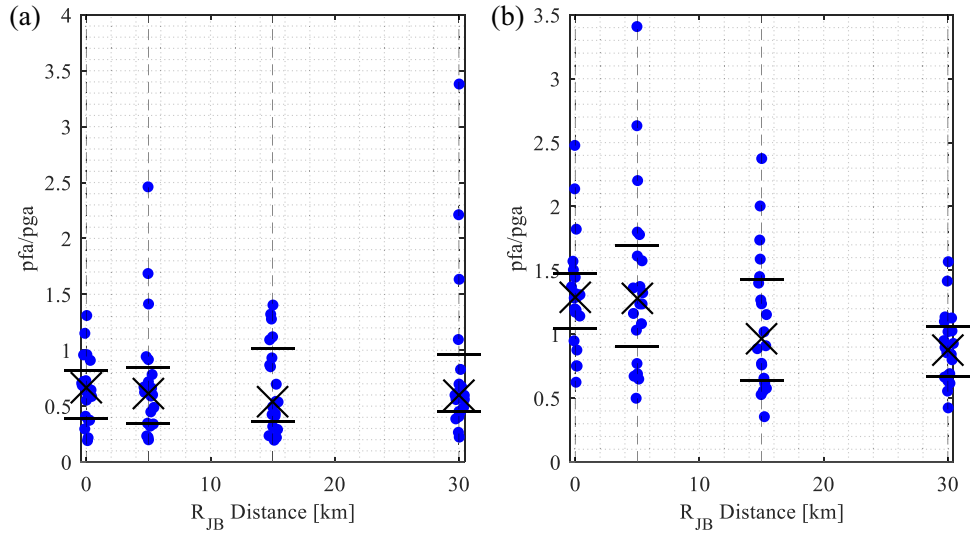

FIGURE 21 | Maximum ratio between pfa and pga in vertical direction for: (a) three-storey and (b) nine-storey superstructures.

horizontal spectra. Based on the findings, the following remarks can be made:

- For the selected near-fault scenario (maximum Mw = 7.4, corresponding to high seismicity in Italy or moderate seismicity in more seismically prone areas), the main near-fault effects, i.e., vertical spectral accelerations at short periods (0.05–0.15 s) exceeding $1 \times g$ and displacement amplification at long periods (4–5 s), disappear for distances to the fault projection greater than $R_{JB} = 5$ km;
- For distances less than or equal to 5 km, particular attention should be paid to the design of structures sensitive to vertical forces of the combined effect of vertical and horizontal forces (such as masonry structures or base-isolated structures), but further investigations are needed for scenarios involving larger magnitudes;
- Current Eurocode 8 (both current version and new draft) lack clear guidelines for defining near-fault response spectra; this code should incorporate advanced ground motion models (GMMs) that account for near-fault effects on both horizontal and vertical components, along with an appropriate procedure for selecting a set of accelerograms that simultaneously match both horizontal and vertical target spectra.

The paper also presents an application to base-isolated structures equipped with HDRBs alone or in combination with FSBs (hybrid isolation system). The results obtained allow the following conclusions to be drawn:

- For both analysed buildings (three- and nine-storey), the design of the isolation system at large distances is conventional; this means that small-diameter HDRBs may be used, either alone or with a small number of sliders; a design shear significantly lower than 2.5 should be assumed to increase the shape factor S_2 so that the buckling load is larger than the axial forces (which are similar with and without the vertical input);

TABLE 12 | Summary of devices in tension or cavitation (HDRBs) or uplift (FSBs) for $R_{JB} = 0$ km.

	Three-storey building		Nine-storey building	
Record number	**HDRB cavitation w/ vert**	**FSBs uplift w/ vert**	**HDRB cavitation w/ vert**	**FSBs uplift w/ vert**
1	12	16	12	2
2	—	—	1	—
3	—	—	1	—
4	—	—	—	—
5	—	—	—	—
6	—	—	—	—
7	—	—	—	—
8	2	—	7	—
9	1	—	2	—
10	2	—	7	—
11	12	16	16	2
12	—	—	—	—
13	—	—	7	2
14	—	—	6	—
15	—	—	—	—
16	—	—	1	—
17	—	—	—	—
18	—	—	—	—
19	—	—	1	—
20	12	16	16	12
N° acc	**6**	**3**	**12**	**4**

TABLE 13 | Summary of devices in tension or cavitation (HDRBs) or uplift (FSBs) for $R_{JB} = 5$ km.

	Three-storey building		Nine-storey building	
Record number	**HDRB cavitation w/ vert**	**FSBs uplift w/ vert**	**HDRB cavitation w/ vert**	**FSBs uplift w/ vert**
1	14	2	20	2
2	12	—	—	—
3	14	4	2	—
4	—	—	—	—
5	—	—	—	—
6	—	—	—	—
7	—	—	—	—
8	—	—	—	—
9	—	—	—	—
10	—	—	—	—
11	—	—	—	—
12	—	—	—	—
13	1	—	7	—
14	—	—	20	4
15	—	—	—	—
16	—	—	—	—
17	—	—	—	—
18	—	—	—	—
19	—	—	—	—
20	—	—	—	—
N° acc	**4**	**2**	**4**	**2**

- Conversely, at distances less than or equal to 5 km, the displacement demand increases significantly, requiring large-diameter HDRBs and a large number of large sliders to maintain total stiffness; due to their large dimensions, the critical loads are also very high, so bearing buckling is not a concern, either with or without the vertical seismic component, thus they can be designed with a shear strain close to 2.5;
- It is confirmed that vertical component does not influence the horizontal response of bearings and does not affect the buckling of bearings nor for small nor for large distance, but it can cause uplift of FSBs and cavitation of HDRBs for a significant number of records, especially for the nine-storey building, where for some devices the effect of the vertical input is combined with the rocking effect due to the horizontal action;
- Additional damping could be introduced at distances less than or equal to 5 km to allow for smaller-diameter bearings. However, in this scenario, the effect of vertical compressive loads could become significant, and the uplift of FSBs and cavitation of HDRBs may potentially worsen;
- Regarding the superstructure, it is confirmed that the vertical input does not affect the horizontal response; however, in the vertical direction, floor accelerations are very high, as confirmed by previous studies, especially for the nine-storey building;
- Current Eurocode 8 (both current version and new draft) lack clear guidelines for base-isolated structures in near-fault (NF) sites; this code should incorporate specific provisions for the design of base-isolated structures located near faults that produce large vertical accelerations (e.g., hanging wall effects in reverse and reverse/oblique faults).

Acknowledgments

This study has been partially developed with the support of the Italian Department of Civil Protection (IDPC), within the ReLUIS-DPC 2024–26 Research Project "Input sismico, normativa e microzonazione" WP18, and "Dispositivi di isolamento e dissipazione" WP15.

Conflicts of Interest

The authors declare no conflicts of interest.

Data Availability Statement

Data will be made available on request.

The waveforms were extracted from the ESM database http://esm-db.eu/#/home.

References

1. J. W. Baker, "Quantitative Classification of Near-Fault Ground Motions Using Wavelet Analysis," *Bulletin of the Seismological Society of America* 97, no. 5 (2007): 1486–1501, https://doi.org/10.1785/0120060255.

2. P. Somerville, "Development of an Improved Representation of Near-fault Ground Motions," in *SMIP98 Proceedings, Seminar on Utilization of Strong-Motion Data* (California Division of Mines and Geology, Sacramento, CA, 1998), https://doi.org/10.1007/1-4020-3812-7.

3. N. Abrahamson, Incorporating Effects of Near-Fault Tectonic Deformation Into Design Ground Motions. University at Buffalo MCEER: Friedman F. V. Professional Program, Webcast (2001).

4. A. Elgamal and L. He, "Vertical Earthquake Ground Motion Records: An Overview," *Journal of Earthquake Engineering* 8, no. 5 (2004): 663–697, https://doi.org/10.1080/13632460409350505.

5. S. K. Shahi and J. W. Baker, A Probabilistic Framework to Include the Effects of Near-Fault Directivity in Seismic Hazard Assessment (*the Dept. of Civil and Environmental Engineering*, Stanford University, Stanford, 2013), https://peer.berkeley.edu/sites/default/files/webpeer-2013-15-shrey_kumar_shahi_and_jack_w._baker.pdf.

6. K. W. Campbell, "Updated Near-Source Ground-Motion (Attenuation) Relations for the Horizontal and Vertical Components of Peak Ground Acceleration and Acceleration Response Spectra," *Bulletin of the Seismological Society of America* 93, no. 3 (2003): 314–331, https://doi.org/10.1785/0120030099.

7. Z. Gülerce and N. A. Abrahamson, "Vector-Valued Probabilistic Seismic Hazard Assessment for the Effects of Vertical Ground Motions on the Seismic Response of Highway Bridges," *Earthquake Spectra* 26, no. 4 (2010): 999–1016, https://doi.org/10.1193/1.3464548.

8. Y. Bozorgnia and K. W. Campbell, "Ground Motion Model for the Vertical-to-Horizontal (V/H) Ratios of PGA, PGV, and Response Spectra," *Earthquake Spectra* 32, no. 2 (2016): 951–978, https://doi.org/10.1193/100614eqs151m.

9. Z. Gülerce, R. Kamai, N. A. Abrahamson, and W. J. Silva, "Ground Motion Prediction Equations for the Vertical Ground Motion Component Based on the NGA-W2 Database," *Earthquake Spectra* 33, no. 2 (2017): 499–528, https://doi.org/10.1193/121814EQS213M.

10. G. Lanzano, L. Luzi, F. Pacor, et al., "A Revised Ground-Motion Prediction Model for Shallow Crustal Earthquakes in Italy," *Bulletin of the Seismological Society of America* 109, no. 2 (2019): 525–540, https://doi.org/10.1785/0120180210.

11. S. Sgobba, C. Felicetta, G. Lanzano, F. Ramadan, M. D'Amico, and F. Pacor, "NESS2.0: An Updated Version of the Worldwide Dataset for Calibrating and Adjusting Ground-Motion Models in near Source," *Bulletin of the Seismological Society of America* 111, no. 5 (2021): 2358–2378, https://doi.org/10.1785/0120210080.

12. F. Ramadan, C. Smerzini, G. Lanzano, and F. Pacor, "An Empirical Model for the Vertical-to-Horizontal Spectral Ratios for Italy," *Earthquake Engineering & Structural Dynamics* 50, no. 15 (2021): 4121–4141, https://doi.org/10.1002/eqe.3548.

13. D. Liberatore, C. Doglioni, O. AlShawa, S. Atzori, and L. Sorrentino, "Effects of Coseismic Ground Vertical Motion on Masonry Constructions Damage During the 2016 Amatrice-Norcia (Central Italy) Earthquakes," *Soil Dynamics and Earthquake Engineering* 120 (2019): 423–435, https://doi.org/10.1016/j.soildyn.2019.02.015.

14. M. Erdik, B. Şadan, C. Tüzün, M. B. Demircioglu-Tumsa, Ö. Ülker, and E. Harmandar, "Near-Fault Earthquake Ground Motion and Seismic Isolation Design," in *Seismic Isolation, Energy Dissipation and Active Vibration Control of Structures*, vol. 309, ed. G. P. Cimellaro (Springer International Publishing, 2023), https://doi.org/10.1007/978-3-031-21187-4_9.

15. F. Mazza and A. Vulcano, "Effects of Near-fault Ground Motions on the Nonlinear Dynamic Response of Base-Isolated R.C. Framed Buildings," *Earthquake Engineering & Structural Dynamics* 41, no. 2 (2012): 211–232, https://doi.org/10.1002/eqe.1126.

16. M. F. Vassiliou, A. Tsiavos, and B. Stojadinović, "Dynamics of Inelastic Base-Isolated Structures Subjected to Analytical Pulse Ground Motions," *Earthquake Engineering & Structural Dynamics* 42, no. 14 (2013): 2043–2060, https://doi.org/10.1002/eqe.2311.

17. J. F. Hall and K. L. Ryan, "Isolated Buildings and the *1997 UBC* Near-Source Factors," *Earthquake Spectra* 16, no. 2 (2000): 393–411, https://doi.org/10.1193/1.1586118.

18. Y. Bao, T. C. Becker, and H. Hamaguchi, "Failure of Double Friction Pendulum Bearings Under Pulse-Type Motions," *Earthquake Engineering & Structural Dynamics* 46, no. 5 (2017): 715–732, https://doi.org/10.1002/eqe.2827.

19. S. Kitayama and M. C. Constantinou, "Performance Evaluation of Seismically Isolated Buildings near Active Faults," *Earthquake Engineering & Structural Dynamics* 51, no. 5 (2022): 1017–1037, https://doi.org/10.1002/eqe.3602.

20. M. Sasani and V. V. Bertero, "Importance of Severe Pulse-Type Ground Motions in Performance-Based Engineering: Historical and Critical," in *Proceedings of the 12th World Conference on Earthquake Engineering, New Zealand Society for Earthquake Engineering, Upper Hutt, New Zealand* vol. 30 (2000).

21. I. D. Aiken, "Recent Developments and Applications of Seismic Isolation in North America," in Proceedings of the 17th World Conference on Seismic Isolation Energy Dissipation and Active Vibration Control of Structures, 17th World Conference on Seismic Isolation (17WCSI) (2022), https://doi.org/10.1007/978-3-031-21187-4.

22. B. Sadan, "State of the Art in Application of Seismic Isolation and Energy Dissipation in Turkey," in Proceedings of the 17th World Conference on Seismic Isolation Energy Dissipation and Active Vibration Control of Structures, 17th World Conference on Seismic Isolation (17WCSI) (2022), https://doi.org/10.1007/978-3-031-21187-4.

23. A. De Luca and L. G. Guidi, "State of Art in the Worldwide Evolution of Base Isolation Design," *Soil Dynamics and Earthquake Engineering* 125 (2019): 105722, https://doi.org/10.1016/j.soildyn.2019.105722.

24. The Japan Society of Seismic Isolation, *Recent Trends of Seismic Isolation "SI" & Vibration Control "VC" Buildings in Japan* (2024).

25. A. A. Sarlis and M. C. Constantinou, Model of Triple Friction Pendulum Bearing for General Geometric and Frictional Parameters and for Uplift Conditions (2013).

26. M. Kumar, A. S. Whittaker, and M. C. Constantinou, "Experimental Investigation of Cavitation in Elastomeric Seismic Isolation Bearings," *Engineering Structures* 101 (2015): 290–305, https://doi.org/10.1016/j.engstruct.2015.07.014.

27. A. A. Sarlis, M. C. Constantinou, and A. M. Reinhorn, *Shake Table Testing of Triple Friction Pendulum Isolators Under Extreme Conditions* (2013).

28. H. Cilsalar and M. C. Constantinou, "Effect of Vertical Ground Motion on the Response of Structures Isolated With Friction Pendulum Isolators," *International Journal of Earthquake and Impact Engineering* 2, no. 2 (2017): 135–157, https://doi.org/10.1504/IJEIE.2017.089048.

29. K. L. Ryan, S. Soroushian, E. Maragakis "Manos," E. Sato, T. Sasaki, and T. Okazaki, "Seismic Simulation of an Integrated Ceiling-Partition Wall-Piping System at E-Defense. I: Three-Dimensional Structural Response and Base Isolation," *Journal of Structural Engineering* 142, no. 2 (2016): 04015130, https://doi.org/10.1061/(ASCE)ST.1943-541X.0001384.

30. F. Mazza and R. Labernarda, "Structural and Non-structural Intensity Measures for the Assessment of Base-Isolated Structures Subjected to

Pulse-Like Near-Fault Earthquakes," *Soil Dynamics and Earthquake Engineering* 96 (2017): 115–127, https://doi.org/10.1016/j.soildyn.2017.02.013.

31. G. Quaranta, G. Angelucci, and F. Mollaioli, "Near-Fault Earthquakes With Pulse-Like Horizontal and Vertical Seismic Ground Motion Components: Analysis and Effects on Elastomeric Bearings," *Soil Dynamics and Earthquake Engineering* 160 (2022): 107361, https://doi.org/10.1016/j.soildyn.2022.107361.

32. D. N. Grant, G. L. Fenves, and A. S. Whittaker, "Bidirectional Modelling of High-Damping Rubber Bearings," *Journal of Earthquake Engineering* 8 (2004): 161–185, https://doi.org/10.1080/13632460409350524.

33. E. Tubaldi, L. Ragni, A. Dall'Asta, H. Ahmadi, and A. Muhr, "Stress Softening Behaviour of HDNR Bearings: Modelling and Influence on the Seismic Response of Isolated Structures," *Earthquake Engineering & Structural Dynamics* 46, no. 12 (2017): 2033–2054, https://doi.org/10.1002/eqe.2897.

34. L. Ragni, E. Tubaldi, A. Dall'Asta, H. Ahmadi, and A. Muhr, "Biaxial Shear Behaviour of HDNR With Mullins Effect and Deformation-Induced Anisotropy," *Engineering Structures* 154 (2018): 78–92, https://doi.org/10.1016/j.engstruct.2017.10.060.

35. M. Kumar, A. S. Whittaker, and M. C. Constantinou, "An Advanced Numerical Model of Elastomeric Seismic Isolation Bearings," *Earthquake Engineering & Structural Dynamics* 43, no. 13 (2014): 1955–1974, https://doi.org/10.1002/eqe.2431.

36. M. Kumar, A. S. Whittaker, and M. C. Constantinou, "Response of Base-Isolated Nuclear Structures to Extreme Earthquake Shaking," *Nuclear Engineering and Design* 295 (2015): 860–874, https://doi.org/10.1016/j.nucengdes.2015.06.005.

37. J. A. Gallardo, M. C. Chen, J. I. Restrepo, and J. C. de la Llera, "Modeling the Multiaxial Behavior of High Damping Rubber Bearings (HDRBs)," *Earthquake Engineering & Structural Dynamics* 54, no. 12 (2025): 3202–3223, https://doi.org/10.1002/eqe.70023.

38. M. C. Constantinou, A. S. Whittaker, Y. Kalpakidis, D. M. Fenz, and G. P. Warn, Performance of Seismic Isolation Hardware Under Service and Seismic Loading (2007).

39. M. Kikuchi and I. D. Aiken, "An Analytical Hysteresis Model for Elastomeric Seismic Isolation Bearings," *Earthquake Engineering & Structural Dynamics* 26, no. 2 (1997): 215–231, https://doi.org/10.1002/(SICI)1096-9845(199702)26:2%3C215::AID-EQE640%3E3.0.CO;2-9.

40. K. Ishii and M. Kikuchi, "Improved Numerical Analysis for Ultimate Behavior of Elastomeric Seismic Isolation Bearings," *Earthquake Engineering & Structural Dynamics* 48, no. 1 (2019): 65–77, https://doi.org/10.1002/eqe.3123.

41. F. Micozzi, A. Flora, L. R. S. Viggiani, D. Cardone, L. Ragni, and A. Dall'Asta, "Risk Assessment of Reinforced Concrete Buildings With Rubber Isolation Systems Designed by the Italian Seismic Code," *Journal of Earthquake Engineering* 26, no. 14 (2021): 7245–7275, https://doi.org/10.1080/13632469.2021.1961937.

42. F. Micozzi, *Seismic Reliability of Buildings Isolated With Rubber Bearings. School of Advanced Studies* (University of Camerino, 2020).

43. G. P. Warn, A. S. Whittaker, and M. C. Constantinou, "Vertical Stiffness of Elastomeric and Lead–Rubber Seismic Isolation Bearings," *Journal of Structural Engineering* 133, no. 9 (2007): 1227–1236, https://doi.org/10.1061/(ASCE)0733-9445(2007)133:9(1227).

44. CEN (European Committee for Standardization), Eurocode 8: Design of Structures for Earthquake Resistance. Part 1: General Rules, Seismic Actions and Rules for Buildings (2005).

45. CEN (European Committee for Standardization), Eurocode 8: Design of Structures for Earthquake Resistance. Part 2: Bridges (2005).

46. ASCE, American Society of Civil Engineers (Reston, Virginia), ed., *ASCE/SEI 7–22. Minimum Design Loads and Associated Criteria for Buildings and Other Structures* (American Society of Civil Engineers, 2022).

47. J. J. Bommer and A. B. Acevedo, "The Use of Real Earthquake Accelerograms as Input to Dynamic Analysis," *Journal of Earthquake Engineering* 8 (2004): 43–91, https://doi.org/10.1080/13632460409350521.

48. I. Iervolino, C. Galasso, and E. Cosenza, "REXEL: Computer Aided Record Selection for Code-Based Seismic Structural Analysis," *Bulletin of Earthquake Engineering* 8, no. 2 (2010): 339–362, https://doi.org/10.1007/s10518-009-9146-1.

49. I. Iervolino, C. Galasso, R. Paolucci, and F. Pacor, "Engineering Ground Motion Record Selection in the ITalian ACcelerometric Archive," *Bulletin of Earthquake Engineering* 9, no. 6 (2011): 1761–1778, https://doi.org/10.1007/s10518-011-9300-4.

50. F. Pacor, C. Felicetta, G. Lanzano, et al., "NESS1: A Worldwide Collection of Strong-Motion Data to Investigate Near-Source Effects," *Seismological Research Letters* 89, no. 6 (2018): 2299–2313, https://doi.org/10.1785/0220180149.

51. C. Chiarabba, L. Jovane, and S. R. Di, "A New Look to the Italian Seismicity: Seismotectonic Inference," *Tectonophysics* 395 (2005): 251–268, https://doi.org/10.1016/j.tecto.2004.09.013.

52. F. Visini, C. Meletti, A. Rovida, V. D'Amico, B. Pace, and S. Pondrelli, "An Updated Area-Source Seismogenic Model (MA4) for Seismic Hazard of Italy," *Natural Hazards and Earth System Sciences* 22, no. 8 (2022): 2807–2827, https://doi.org/10.5194/nhess-22-2807-2022.

53. F. Visini, B. Pace, C. Meletti, et al., "Earthquake Rupture Forecasts for the MPS19 Seismic Hazard Model of Italy," *Annals of Geophysics* 64, no. 2 (2021): SE220, https://doi.org/10.4401/ag-8608.

54. L. Luzi, G. Lanzano, C. Felicetta, et al., Engineering Strong Motion Database (ESM), Version 2.0 (2020), https://doi.org/10.13127/ESM.2.

55. R. Puglia, E. Russo, L. Luzi, et al., "Strong-Motion Processing Service: A Tool to Access and Analyse Earthquakes Strong-Motion Waveforms," *Bulletin of Earthquake Engineering* 16, no. 7 (2018): 2641–2651, https://doi.org/10.1007/s10518-017-0299-z.

56. D. M. Boore, "Orientation-Independent, Nongeometric-Mean Measures of Seismic Intensity From Two Horizontal Components of Motion," *Bulletin of the Seismological Society of America* 100, no. 4 (2010): 1830–1835, https://doi.org/10.1785/0120090400.

57. S. Sgobba, R. Puglia, F. Pacor, et al., "REXELweb: A Tool for Selection of Ground-Motion Records From the Engineering Strong Motion Database (ESM)," *Earthquake Geotechnical Engineering for Protection and Development of Environment and Constructions* (CRC Press, 2019).

58. F. Scozzese, E. Tubaldi, and A. Dall'Asta, "Assessment of the Effectiveness of Multiple-Stripe Analysis by Using a Stochastic Earthquake Input Model," *Bulletin of Earthquake Engineering* 18, no. 7 (2020): 3167–3203, https://doi.org/10.1007/s10518-020-00815-1.

59. D. N. Grant, "Response Spectral Matching of Two Horizontal Ground-Motion Components," *Journal of Structural Engineering* 137, no. 3 (2011): 289–297, https://doi.org/10.1061/(ASCE)ST.1943-541X.0000227.

60. NTC, Aggiornamento delle "Norme Tecniche per le costruzioni" (in Italian) (2018).

61. N. Luco and P. Bazzurro, "Effects of Earthquake Record Scaling on Nonlinear Structural Response," in *Rep on PEER-LL Program Task 1G00, Addendum (Sub-Task 1 of 3)* (2004), https://apps.peer.berkeley.edu/lifelines/lifelines_pre_2006/final_reports/1G00-FR.pdf.

62. P. Bordoni, S. Gori, A. Akinci, et al., "A Site-Specific Earthquake Ground Response Analysis Using a Fault-Based Approach and Nonlinear Modeling: The Case Pente Site (Sulmona, Italy)," *Engineering Geology* 314 (2023): 106970, https://doi.org/10.1016/j.enggeo.2022.106970.

63. F. Micozzi, F. Scozzese, L. Ragni, and A. Dall'Asta, "Seismic Reliability of Base Isolated Systems: Sensitivity to Design Choices," *Engineering Structures* 256 (2022): 114056, https://doi.org/10.1016/j.engstruct.2022.114056.

64. M. Kohrangi, S. R. Kotha, and P. Bazzurro, "Ground-Motion Models for Average Spectral Acceleration in a Period Range: Direct and Indirect Methods," *Bulletin of Earthquake Engineering* 16, no. 1 (2018): 45–65, https://doi.org/10.1007/s10518-017-0216-5.

65. S. K. Shahi and J. W. Baker, "An Empirically Calibrated Framework for Including the Effects of Near-Fault Directivity in Probabilistic Seismic Hazard Analysis," *Bulletin of the Seismological Society of America* 101, no. 2 (2011): 742–755, https://doi.org/10.1785/0120100090.

66. CEN (European Committee for Standardization), EN 15129:2010 - Antiseismic Devices (2010).

67. F. Micozzi, L. Ragni, L. Gioiella, V. Quaglini, and A. Dall'Asta, "Variability of Dynamic Properties of Rubber Compounds for Elastomeric Bearings," *Structural Control and Health Monitoring* 2023 (2023): 1–17, https://doi.org/10.1155/2023/6638748.

68. H. Kim and M. C. Constantinou, "Performance-Based Testing Specifications for Seismic Isolators," *Earthquake Engineering & Structural Dynamics* 52, no. 15 (2023): 5141–5161, https://doi.org/10.1002/eqe.4006.

69. A. Dall'Asta, G. Leoni, L. Gioiella, et al., "Push-and-Release Tests of a Steel Building With Hybrid Base Isolation," *Engineering Structures* 272 (2022): 114971, https://doi.org/10.1016/j.engstruct.2022.114971.

70. CEN (European Committee for Standardization), Eurocode 1: Actions on Structures. Part 1–4: General Actions—Wind Actions (2004).

71. CEN (European Committee for Standardization), Eurocode 2: Design of Concrete Structures. Part 1-1: General Rules and Rules for Buildings (1992).

72. CSI, SAP2000 Integrated Software for Structural Analysis and Design (2019).

73. F. McKenna, G. Fenves, and M. Scott, OpenSees: Open System for Earthquake Engineering Simulation (University of California, Berkeley, 2006).

74. K. Ishii and M. Kikuchi, "Improved Numerical Analysis for Ultimate Behavior of Elastomeric Seismic Isolation Bearings," *Earthquake Engineering & Structural Dynamics* 48, no. 1 (2019): 65–77, https://doi.org/10.1002/eqe.3123.

75. C. G. Koh and J. M. Kelly, *Effects of Axial Load on Elastomeric Bearings* (University of California, 1986).

76. C. G. Koh and J. M. Kelly, "A Simple Mechanical Model for Elastomeric Bearings Used in Base Isolation," *International Journal of Mechanical Sciences* 30, no. 12 (1988): 933–943, https://doi.org/10.1016/0020-7403(88)90075-6.

77. M. Kikuchi and I. D. Aiken, "An Analytical Hysteresis Model for Elastomeric Seismic Isolation Bearings," *Earthquake Engineering & Structural Dynamics* 26 (1997): 215–231, https://doi.org/10.1002/(SICI)1096-9845(199702)26:2%3C215::AID-EQE640%3E3.0.CO;2-9.

78. M. Constantinou, A. Mokha, and A. Reinhorn, "Teflon Bearings in Base Isolation II: Modeling," *Journal of Structural Engineering* 116, no. 2 (1990): 455–474, https://doi.org/10.1061/(ASCE)0733-9445(1990)116:2(455).

79. V. Quaglini, E. Gandelli, and P. Dubini, "Experimental Investigation of the Re-Centring Capability of Curved Surface Sliders," *Structural Control and Health Monitoring* 24, no. 2 (2017): e1870, https://doi.org/10.1002/stc.1870.

80. D. Cardone, A. Flora, and G. Gesualdi, "Inelastic Response of RC Frame Buildings With Seismic Isolation," *Earthquake Engineering & Structural Dynamics* 42, no. 6 (2013): 871–889, https://doi.org/10.1002/eqe.2250.

81. D. Cardone, N. Conte, and A. Dall'Asta, et al., "Rintc Project: Nonlinear Analyses of Italian Code-Conforming Base-Isolated Buildings for Risk of Collapse Assessment," in *Proceedings of the 6th International Conference on Computational Methods in Structural Dynamics and Earthquake Engineering (COMPDYN 2015)* (Institute of Structural Analysis and Antiseismic Research School of Civil Engineering National Technical University of Athens (NTUA) Greece, 2017), https://doi.org/10.7712/120117.5525.19365.

82. D. Cardone and A. Flora, "An Alternative Approach for the Seismic Rehabilitation of Existing RC Buildings Using Seismic Isolation," *Earthquake Engineering & Structural Dynamics* 45, no. 1 (2016): 91–111, https://doi.org/10.1002/eqe.2618.

83. P. Ricci, V. Manfredi, F. Noto, et al., "Modeling and Seismic Response Analysis of Italian Code-Conforming Reinforced Concrete Buildings," *Journal of Earthquake Engineering* 22, no.S2 (2018): 105–139, https://doi.org/10.1080/13632469.2018.1527733.

84. L. F. Ibarra, R. A. Medina, and H. Krawinkler, "Hysteretic Models That Incorporate Strength and Stiffness Deterioration," *Earthquake Engineering & Structural Dynamics* 34, no. 12 (2005): 1489–1511, https://doi.org/10.1002/eqe.495.

85. L. F. Ibarra and H. Krawinkler, *Global Collapse of Frame Structures under Seismic Excitations, PEER Report 2005-06*. Pacific Earthquake Engineering Research Center, University of California, Berkeley, CA. (2005) .

86. L. D. Decanini, F. Mollaioli, A. Mura, and R. Saragoni, "Seismic Performance of Masonry Infilled R/c Frames," in *Proceedings of the 13th World Conference on Earthquake Engineering*, Vancouver, B. C., Canada (2004).

87. K. Sassun, T. J. Sullivan, P. Morandi, and D. Cardone, "Characterising the In-Plane Seismic Performance of Infill Masonry," *Bulletin of the New Zealand Society for Earthquake Engineering* 49, no. 1 (2016): 98–115, https://doi.org/10.5459/bnzsee.49.1.98-115.

88. L. D. Decanini, L. Liberatore, and F. Mollaioli, "Strength and Stiffness Reduction Factors for Infilled Frames With Openings," *Earthquake Engineering and Engineering Vibration* 13, no. 3 (2014): 437–454, https://doi.org/10.1007/s11803-014-0254-9.

89. K. L. Ryan and J. Polanco, "Problems With Rayleigh Damping in Base-Isolated Buildings," *Journal of Structural Engineering* 134, no. 11 (2008): 1780–1784, https://doi.org/10.1061/(ASCE)0733-9445(2008)134:11(1780).

90. D. R. Pant, A. C. Wijeyewickrema, and M. A. ElGawady, "Appropriate Viscous Damping for Nonlinear Time-history Analysis of Base-isolated Reinforced Concrete Buildings," *Earthquake Engineering & Structural Dynamics* 42, no. 15 (2013): 2321–2339, https://doi.org/10.1002/eqe.2328.

91. H. Anajafi, R. A. Medina, and E. Santini-Bell, "Effects of the Improper Modeling of Viscous Damping on the First-Mode and Higher-Mode Dominated Responses of Base-Isolated Buildings," *Earthquake Engineering & Structural Dynamics* 49, no. 1 (2020): 51–73, https://doi.org/10.1002/eqe.3223.

92. J. McCormick, H. Aburano, M. Ikenaga, and M. Nakashima, "Permissible Residual Deformation Levels for Building Structures Considering both Safety and human Elements," in *Proceedings of the 14th World Conference on Earthquake Engineering* (Seismological Press, Beijing, 2008).

93. Applied Technology Council, *Seismic Performance Assessment of Buildings* (2012).